# OPTICAL TRANSMISSION THROUGH NANOHOLE ARRAYS

by

Brian Leathem

BSc. Simon Fraser University, 2001

THESIS SUBMITTED IN PARTIAL FULFILLMENT

OF THE REQUIREMENTS FOR THE DEGREE OF

MASTER OF SCIENCE

IN THE DEPARTMENT

OF

PHYSICS



SIMON FRASER UNIVERSITY

June 2004

# APPROVAL

**Name:** Brian Leathem

**Degree:** M.Sc.

**Title of Thesis:** Optical Transmission Through Nanohole Arrays

**Examining Committee:** Dr. Howard Trottier (Chair)

---

Dr. Karen Kavanagh (Senior Supervisor)
Professor, Department of Physics

---

Dr. John Bechhoefer
Professor, Department of Physics

---

Dr. Simon Watkins
Professor, Department of Physics

---

Dr. Mike Thewalt
Internal Examiner
Professor, Department of Physics

**Date Approved:** May 27th, 2004

# SIMON FRASER UNIVERSITY

## Partial Copyright Licence

# Abstract

An enhanced optical transmission is observed through metal films containing a periodic array of subwavelength-diameter holes. The transmission spectra show well-defined maxima and minima, which are respectively attributed to surface plasmons and Woods anomalies. A strong polarization dependence of the transmitted light on the ellipticity and orientation of the holes is observed; the polarization axis lies perpendicular to the broad edge of the ellipse. A comparison was made of the transmission through an array with a basis of single or double holes. When aligned to the lattice vector of the array, the two bases give similar results. However, upon rotation of the basis, the amplitude and polarization of the surface plasmon resonance show very different behavior. By studying the effect of the shape and number of elements in the basis, further insight is gained into the surface-plasmon mode coupling to the incident electromagnetic fields, via the periodic array of nano-holes.

*For my wife, whose patience has been infinite and whose support has been endless.*

# Acknowledgments

I would like to express my gratitude my supervisor, Dr. Karen Kavanagh, for allowing me the freedom and guidance to explore the many facets of experimental physics.

I would like to thank Dr. Reuven Gordon from the Department of Electrical and Computer Engineering at the University of Victoria, and Dr. Alexandre G. Brolo from the Department of Chemistry also at the University of Victoria, for their contributions to this thesis. Their ideas and leadership were instrumental to both the origin and completion of this work.

Dr. Li Yang was invaluable in the work she does maintaining the electron microscopes. Scott Wilson was always ready to help design and build various hardware, necessary for the advancement of various projects. Paul Chafe and Aron Mckinnon both did summer projects that laid some important groundwork for my thesis.

A special thank you goes out to my parents, for their continuous words of support.

I am also grateful for funding support from the National Science and Engineering Research Council and to the Canadian Institution for Photonics Innovation.

# Contents

# List of Tables

# List of Figures

# Chapter 1

# Introduction

In 1944, Hans A. Bethe wrote a Physical Review article titled the "Theory of Diffraction by Small Holes" [1] which has, up until recently, been accepted as the standard article for the transmissivity of apertures smaller than the wavelength of the incident light. This fundamental constraint on the manipulation of light predicts that the transmission efficiency of a sub-wavelength "nanohole", of radius $a$, scales as

$$(a/\lambda)^4 \tag{1.1}$$

where $\lambda$ is the light's wavelength. However, it turns out that if the nanoholes are arranged in a two-dimensional lattice, and the film is conductive, then the transmissivity is dramatically increased by over three orders of magnitude [2] when compared to the summed "Bethe" contribution of the individual holes.

## 1.1 Enhanced Transmission Through Arrays of Nanoholes

The enhancement in the transmission of light through a nanohole grating was discovered by Ebbesen et al. [3] in 1998. It provides a means of manipulating light at size scales smaller than its wavelength, and the possibility of numerous novel photonic devices exploiting this enhancement is immediately recognizable, from photonic switching to biosensing applications [2]. In their first paper [3], and in all subsequent papers [4–11], Ebbesen et al. attributed the enhancement effect to the coupling of light with surface plasmons, which are collective excitations of the electron density. By comparing the absolute transmission

efficiency (the fraction of light transmitted) to the fraction of the surface opened up by the holes, they concluded that the array of nanoholes is an active element in the transmission. The ratio of these two quantities is larger than unity, indicating that more light is transmitted than is incident upon the holes. In addition, this transmission efficiency scales linearly with the hole diameter, in stark contrast to the Bethe prediction (eq. 1.1).

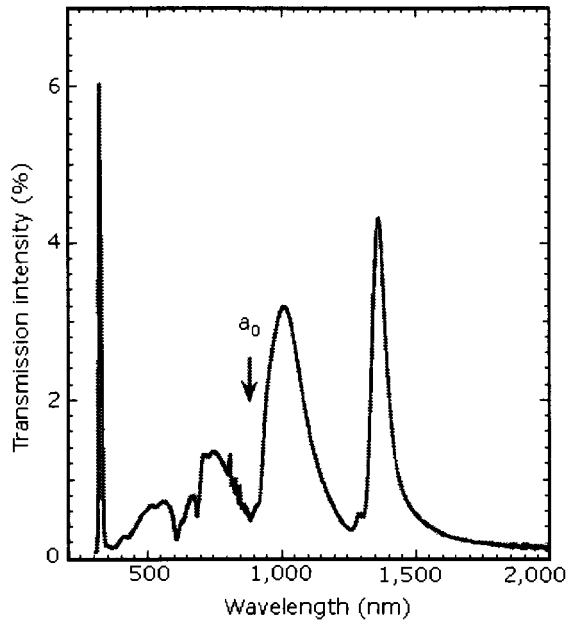


Figure 1.1: Zero-order transmission spectrum of an Ag array [3]. The lattice spacing $a_0$ is 900 nm, marked by an arrow, and the holes diameter is 150 nm. The narrow peak at 326 nm is the bulk plasmon peak, which disappears at thicker film thicknesses. This is the first spectrum published by Ebbesen showing the enhancement effect.

A transmission spectrum showing the enhancement effect for an array of Ag nanoholes is presented in Fig. 1.1. The narrow peak observed at $\lambda = 326$ nm comes from the bulk plasmons, and the remaining peaks originate from the transmission enhancement associated with the nanohole array. The wavelength of the peaks in the transmission spectrum are determined by the lattice spacing of the array, not by the hole size. The asymmetry of the peaks is described by the Wood's anomaly, which is a common observation in diffraction gratings. The Wood's anomaly occurs when a diffracted order becomes tangent to the

grating. The light from this disappeared diffraction order gets re-distributed among the remaining orders. This forbidden diffraction order extinguishes transmission for a particular wavevector, and occurs at wavelengths just below the surface plasmon resonance. This results in a dip on the low wavelength side of each enhancement peak [3].

The dispersion curve of the surface plasmons was also studied [4]. The momentum transferred to the surface plasmon varies with the angle of the incident light. By measuring the transmission intensity as a function of the angle of incidence, profiles of the dispersion curve of the surface plasmons have been created. This technique was further refined using a near-field scanning optical microscope (NSOM) [4] to map out the intensity in the plane of the film. These maps of the dispersion curve show the presence of an energy gap. The NSOM technique also demonstrated that the light transmission was concentrated at the holes themselves, not in the area between.

### 1.1.1 Characteristics of the Transmission Enhancement

Many of the characteristics, and variations of this enhancement effect have been studied, some of which will be outlined below. Focusing on zero-order (on-axis) transmission, the effect of the lattice size and geometry was investigated [5]. For instance, using a hexagonal array of nanoholes, as opposed to a square array showed the importance of nearest neighbor distances between the holes. Investigations of the number of elements in the array showed that, although quite weak, the enhancement can be observed with as few as seven holes in a "micro-array".

A free-standing film was used to investigate the crucial role the metal surface plays in the transmission enhancement [6]. Making a nanohole array on a poor metal such as nickel, results in a very weak enhancement effect. The quality of a metal is characterized by the ratio of the real part of its dielectric function to the imaginary part. If the magnitude of this ratio is much greater than one, then the metal is considered a good candidate for surface plasmon excitation. By coating the free-standing nickel film with a "good" metal like silver, one observes a dramatic increase in the enhancement effect. This demonstrated that the enhancement effect depends strongly on the surface of the metal film and is not purely a diffraction or geometrical effect.

One of the first theoretical publications on the enhancement effect came in 2001 [7].

A fully three-dimensional theory was developed that showed the enhancement to be due to tunneling through surface plasmon states. This tunneling between states can be broken down into two regimes, depending on whether or not the film is thin enough for the plasmon states on either side to interact with one another. This two-regime tunneling scenario was tested experimentally in a subsequent paper [8], where the effect of varying the hole depth, or the film thickness, was investigated. For deep holes, where the two surface plasmons are uncoupled, the transmission decays exponentially with increasing thickness. In thin films, where the hole depth is shallow, the surface plasmons modes on either side of the film couple, and at sufficiently thin film thicknesses, this tends to broaden the peak.

It is interesting to note that the periodic pattern does not have to be an array of nanoholes to produce the enhancement. The enhancement effect was also observed using a bull's eye pattern [9]. In fact, only the center of the bull's-eye pattern was milled all the way through, the surrounding circles were only partially milled; yet the enhancement was still observed. It should be noted that although the ring pattern was not milled all the way through, it was present on both sides of the film. This effect was also achieved with gratings, where only the center line was milled all the way through.

Studies were made of the transmission of individual sub-wavelength holes using the NSOM technique [12]. This showed that the direction of surface-plasmon propagation follows the polarization of the incident light. The directionality of the surface-plasmon propagation has been applied in a novel photonic device [10]. Two arrays of nanoholes were created, one "source" array, and one "probe array". A pump beam was used to illuminate the source array. Surface plasmons travelled to the probe array, and emitted light. Since the direction of surface-plasmon propagation followed the polarization of the incident light, one could switch between different probe arrays, by varying the polarization of the incident light.

In addition to the transmission through nanohole arrays, the reflection and absorption have also been measured [11]. These measurements show that a transmittance peak is associated with a reflectivity minimum, and an absorbance maximum. This increased absorbance comes from the damping of the surface plasmons coupling to the incident light. Similarly for low transmission, the reflectivity is high, and the absorption low. In this case, surface plasmons are not coupling to the incident light, and their damping does not come into play.

An effect first noticed by Wood in the early 20th century [13], while studying diffraction from metallic gratings, is crucial to the understanding of the transmission spectra. The effect occurs when a diffracted order becomes tangent to the plane of the grating, and is known as the Wood's or Rayleigh anomaly. Some have claimed that the enhancement effect can be explained purely by Wood anomalies [13], since the coupling of light to surface plasmons is also known as Resonant Woods anomalies. Using this formalism, Sarrazin et al. have developed a theory, which involves solving Maxwell's equations using a Fourier-series approach. The results match well with experimental data.

The effect of the hole shape is either overlooked or ignored in most publications. While many groups have studied nanowire gratings, the physics learned from these experiments should be applied to the nanohole experiment with extreme care, as the physics is different. For instance, nanowires can always support propagating modes, whereas sufficiently small nanoholes do not [11]. The lack of study on the effect of the hole shape is evidence of how little is known about surface-plasmon behavior. In at least one theoretical paper, it is explicitly stated that the transmission is independent of the hole shape [7]. This is a rather surprising assumption, and should be verified experimentally.

### 1.1.2 Surface-Plasmon-Enhanced Diffraction

In their most recent paper [11], Ebbesen et al. present the idea that the enhancement effect is caused by surface-plasmon-enhanced *diffraction*. If we consider light incident on an array of nanoholes, the light is diffracted by the array, producing evanescent waves. Since sub $\lambda/2$ holes cannot support propagating modes, the evanescent waves tunnel through the holes. This results in evanescent waves on the backside of the metal film, although of considerably smaller amplitude. These evanescent waves then scatter off the array of nanoholes, resulting in propagating light, that has been "transmitted" through the film. The role of the surface plasmons is to greatly enhance the magnitude of the evanescent waves on both the front and back side of the metal film - hence the great increase in transmission. The key to the idea is that diffraction is central to the process and is enhanced by the involvement of surface plasmons. Recall that the enhancement through a nickel film is augmented by overcoating the film with silver [6]. When the surface plasmons are excited, they intensely magnify the strength of the evanescent fields and hence the increased transmission.

### 1.1.3 Electron-Excited Surface Plasmons

Surface plasmons can also be excited by electrons. The mass of the electron allows surface plasmons to be excited under a wider range of conditions than photons, while still conserving momentum. In order to probe optical emission from electron-excited surface plasmons, various groups have collected the light emitted from a Scanning Tunneling Microscope (STM) as it scans various surfaces. This modification to the STM was originally realized by Schlittler et al. [14], when they detected the light emitted in an STM as the tip scanned a silver surface. It is believed that the excitation and decay of surface plasmons on the surface was the cause of the light generation. Light emission in an STM was later also measured by Alvarado et al. [15] from STM scans of III-V heterostructures, in their study of cathodoluminescence.

## 1.2 Thesis Objectives

The initial objective of this thesis was to study light emission of surface plasmons generated by tunneling electrons in an STM. An existing commercial STM was modified with the apparatus necessary to collect light emitted (STM-LE) during tunneling. The influence of nanostructures on the efficiency of light generation was then to be studied.

A second objective of this thesis was to fabricate nanohole arrays using a focused ion beam, and to investigate the role of the hole, or array basis, shape and constitution on the enhanced optical transmissivity through the metal films.

This thesis will begin with a derivation of the surface plasmon dispersion relation, as it is at the root of surface plasmon measurement techniques. Following this, the STM-LE system designed and tested are described; however, tunneling induced light emission was not detected. An evaluation of reasons for this failure and recommendations for future designs are considered. The optical experiment is then described, from the fabrication of the nanohole arrays to the measurement of the optical transmission. The idea of surface-plasmon-enhanced diffraction is investigated through the use of Fourier analysis of the nanohole gratings, in an attempt to see whether they can correctly predict the trends observed experimentally.

# Chapter 2

# Plasmons

A plasma is defined as a medium with equal concentration of positive and negative charges, where at least one of the two types of charges is mobile [16]. A conductive solid satisfies this condition, with mobile conduction electrons moving over a background of positive ions.

## 2.1 Bulk Plasmons

The equation of motion for a free electron, of mass $m$ and charge $-e$ moving in an electric field $E$, is

$$m\frac{d^2x}{dt^2} = -eE \tag{2.1}$$

By solving this equation, one can derive the frequency of oscillation of electrons in a conductor, which is known as the plasma frequency, $\omega_p$,

$$\omega_p = \sqrt{\frac{4\pi ne^2}{m}} \tag{2.2}$$

where $n$ is the electron density. Using the plasma frequency, we can write the dielectric function as [16]

$$\varepsilon = 1 - \frac{\omega_p^2}{\omega^2}. \tag{2.3}$$

The dispersion relation for an electron of wavevector $\vec{k}$ is

$$\varepsilon\left(\frac{\omega}{c}\right)^2 = |\vec{k}|^2, \tag{2.4}$$

which involves the dielectric function ε [16]. Combining equations (2.3) and (2.4) gives

$$\omega^2 - \omega_p^2 = c^2|\vec{k}|^2. \tag{2.5}$$

From eq. (2.5), we can see that for $\omega < \omega_p$, $k$ is imaginary, and we have no propagating optical modes in the metal. However, for $\omega > \omega_p$, propagating optical modes exist, and the metal becomes transparent.

At the plasma frequency, there exists a plasma oscillation mode, a longitudinal density fluctuation of the plasma in the volume of the metal [17]. The quantum of this plasma oscillation is called a "bulk plasmon". Bulk plasmons have a single discrete energy $E_p$, related to the plasma frequency, $E_p = \hbar\omega_p$ [17].

## 2.2 Surface Plasmons

A solution of Maxwell's equation on the surface of a metal shows propagating electromagnetic waves. These waves are surface plasmons, also known as "surface plasma polaritons" [17]. The electro-magnetic field associated with the collective electron oscillation is why surface plasmons are often referred to as "surface plasma polaritons".

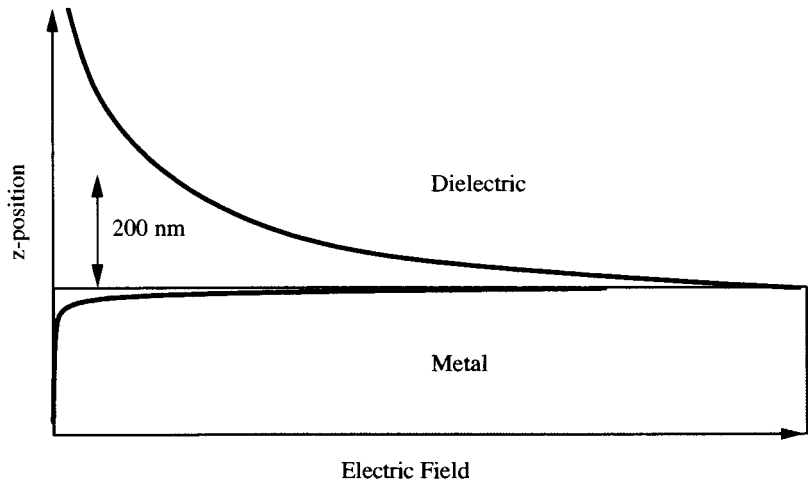


Figure 2.1: Magnitude of the electric field associated with surface plasmons

Unlike bulk plasmons, which are confined to a single energy, surface plasmons have states with eigenfrequencies from 0 to $\omega_p/\sqrt{2}$. They propagate along the surface, and are

localized in the $z$-direction [17]. The localization in the z-direction is demonstrated in Fig. 2.1 where the electric field decays much more quickly in the metal than in the dielectric.

### 2.2.1 Surface Plasmon Dispersion Relation

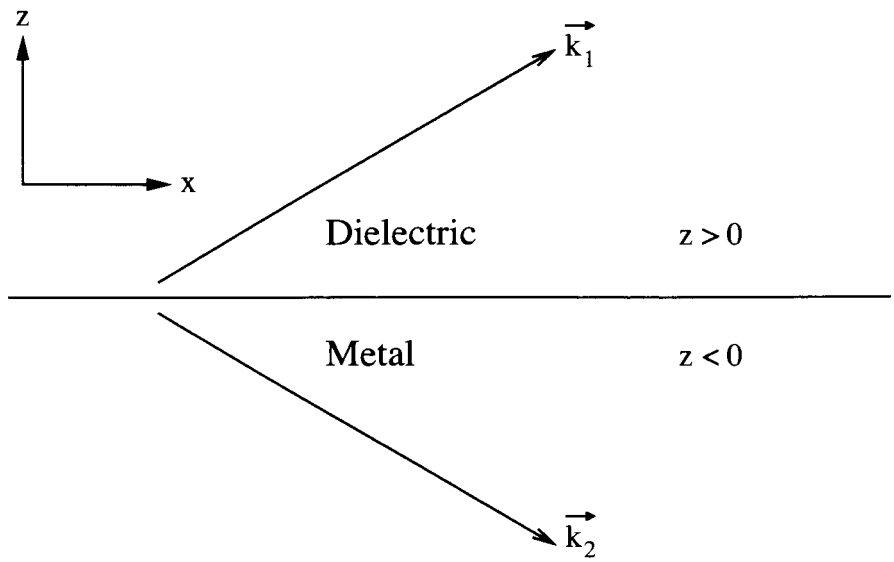


Figure 2.2: Wave vectors of the electric field at the interface between two media 1 and 2. By solving Maxwell's equations (eqs. 2.8) and applying the appropriate boundary conditions (eqs. 2.10), the x-component of the wave vector is found to be continuous across the interface, and the imaginary z-component confines the field to the interface.

The dispersion relation for surface plasmons can be derived from the electromagnetic wave, which describes the propagation of the surface plasmon. In the equations below, x is taken as the direction of propagation along the interface in the metal surface, and the $z$-direction is perpendicular to the metal surface. The electromagnetic fields in each of the two regions of Fig. 2.2, air(1) and metal(2), are given by

$$\begin{aligned} \textit{metal}: \quad z<0 \quad \vec{H}_2 &= (0,H_{y2},0)\, e^{i(k_{x2}x + k_{z2}z - \omega t)} \\ \vec{E}_2 &= (E_{x2},0,E_{z2})\, e^{i(k_{x2}x + k_{z2}z - \omega t)} \\ \textit{air}: \quad z>0 \quad \vec{H}_1 &= (0,H_{y1},0)\, e^{i(k_{x1}x - k_{z1}z - \omega t)} \end{aligned} \tag{2.6}$$

$$\vec{E}_1 = (E_{x1}, 0, E_{z1})\, e^{i(k_{x1}x - k_{z1}z - \omega t)} \tag{2.7}$$

where $\vec{E}$ and $\vec{H}$ are the electric and magnetic field vectors of the propagating electromagnetic wave. The relevant Maxwell equations are,

$$\vec{\nabla} \times \vec{H}_i = \varepsilon_i \frac{1}{c}\frac{\partial}{\partial t}\vec{E}_i \tag{2.8}$$

$$\vec{\nabla} \times \vec{E}_i = -\frac{1}{c}\frac{\partial}{\partial t}\vec{H}_i \tag{2.9}$$

and the boundary conditions are

$$\begin{aligned} E_{x1} &= E_{x2} \\ H_{y1} &= H_{y2} \\ \varepsilon_1 E_{z1} &= \varepsilon_2 E_{z2}. \end{aligned} \tag{2.10}$$

The boundary conditions (2.10) ensure the continuity of the wavevector in the $x$-direction

$$k_{x1} = k_{x2} = k_x. \tag{2.11}$$

Applying Maxwell's equation (2.8) to the field equations (2.6) and (2.7) yields

$$\begin{aligned} (k_{z1}H_{y1}, 0, k_{x1}H_{y1}) &= (-\frac{\omega}{c}\varepsilon_1 E_{x1}, 0, -\frac{\omega}{c}\varepsilon_1 E_{z1}) \\ (k_{z2}H_{y2}, 0, k_{x2}H_{y2}) &= (\frac{\omega}{c}\varepsilon_2 E_{x2}, 0, -\frac{\omega}{c}\varepsilon_2 E_{z2}). \end{aligned} \tag{2.12}$$

Equating the $x$-components of equations of the above equations gives [1]

$$\begin{aligned} k_{z1}H_{y1} &= -\frac{\omega}{c}\varepsilon_1 E_{x1} \\ k_{z2}H_{y2} &= +\frac{\omega}{c}\varepsilon_2 E_{x2}. \end{aligned} \tag{2.13}$$

Solving this system of equations together with the first two boundary conditions (2.10) yields the dispersion relation for surface plasmons,

$$\frac{k_{z1}}{\varepsilon_1} + \frac{k_{z2}}{\varepsilon_2} = 0. \tag{2.14}$$

[1] The right-hand side of these equations in [17] have a sign error.

Furthermore, if we apply the second of Maxwell's equations (2.9) to the field equations,

$$\begin{aligned}(0,-k_{x1}E_{z1}-k_{z1}E_{x1},0) &= (0,\frac{\omega}{c}H_{y1},0)\\ (0,-k_{x2}E_{z2}+k_{z2}E_{x2},0) &= (0,\frac{\omega}{c}H_{y2},0),\end{aligned} \tag{2.15}$$

the components of these form a system of equations, which when combined with eqs. (2.12) and the boundary conditions (2.10), give the result

$$k_x^2+k_{zi}^2=\varepsilon_i\left(\frac{w}{c}\right)^2. \tag{2.16}$$

This is analogous to the result for bulk plasmons (eq. 2.4), and when combined with the dispersion relation (eq. 2.14), we get the result

$$k_x=\frac{w}{c}\sqrt{\frac{\varepsilon_1\varepsilon_2}{\varepsilon_1+\varepsilon_2}}. \tag{2.17}$$

### 2.2.2 Surface-Plasmon Excitation and Decay

Surface plasmons propagate along the surface. They can decay either thermally, or radiatively under certain conditions. Surface plasmons are relatively easy to excite using electrons impinging on a metal surface. Consider an electron with wavevector $k_{el}$ incident upon a metal film. It scatters off the film at an angle $\theta$ and transfers momentum $\hbar q$ and energy $\Delta E$ to the film. (See Fig. 2.3a) This transferred momentum and energy can excite a surface plasmon with wavevector $k_sp = k_x$, the x-component of the transferred wavevector $q$.

Exciting surface plasmons optically, however, is not as straightforward. Light does not couple to plasmons on a smooth metal-air interface [4]. Since the dispersion curve lies to the right of the light line, the photon momentum is insufficient to excite a surface plasmon. One way to overcome this momentum deficiency is to couple the light to the surface plasmon through a grating. In this way, some of the momentum associated with the periodic structure of the array allows the light to interact with the surface plasmon, while still conserving momentum [5]. If the incident radiation scatters, it can transfer a wavevector $q$ to the film [17]. The projection of this wavevector on the surface is

$$k_x=\frac{\omega}{c}\sin(\theta_0)=\frac{2\pi}{\lambda}\sin(\theta_0) \tag{2.18}$$

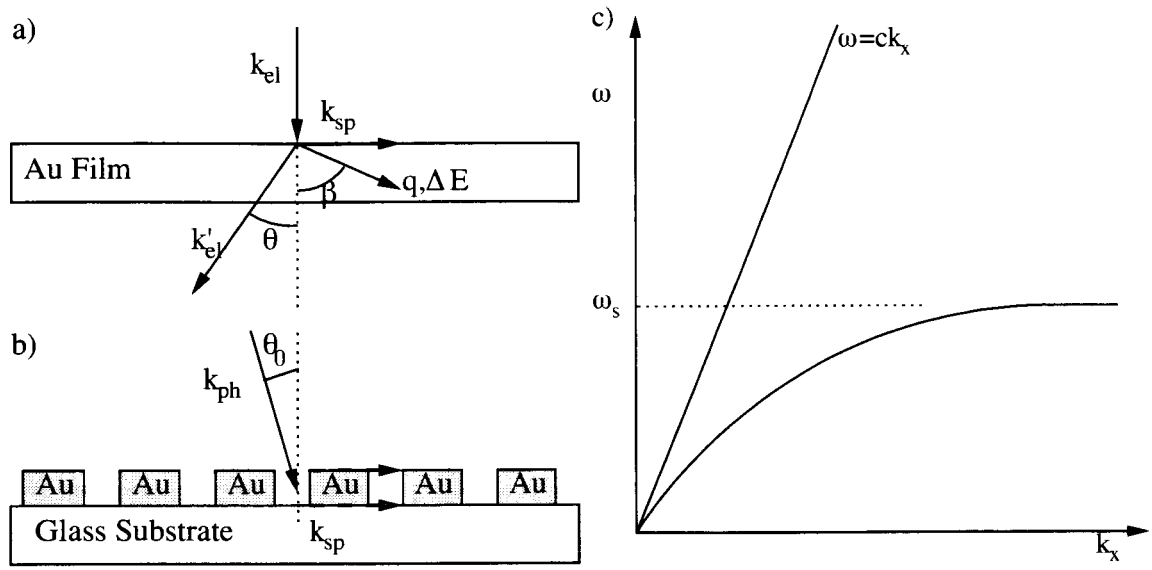


Figure 2.3: a) A surface plasmon excited by an electron at normal incidence. b) A surface photon incident at an angle $\theta_0$ coupled to a surface plasmon via a periodic grating (as in eq. 2.20). c) The dispersion curve of surface plasmons (eq. 2.14) to the right of the light line, $\omega = ck_x$ [17].

In the presence of a grating, momentum is conserved according to the equation

$$\vec{k}_{sp} = \vec{k}_x + \vec{G} \tag{2.19}$$

where the wavevector is augmented by a reciprocal lattice vector, $\vec{G}$. For a two-dimensional grating, we have

$$\vec{k}_{sp} = \vec{k}_x + i\vec{G}_x + j\vec{G}_y \tag{2.20}$$

where $i$ and $j$ are integers, and for a square lattice of spacing $a_0$, $G_x = G_y = \frac{2\pi}{a_0}$. By invoking the dispersion relation (eq. 2.17) we get the following equation for a two dimensional grating:

$$|\vec{k}_{sp}| = \left[\left(\frac{2\pi}{\lambda}\sin(\theta_0) + i\frac{2\pi}{a_0}\right)^2 + \left(j\frac{2\pi}{a_0}\right)^2\right]^{1/2} = \frac{w}{c}\sqrt{\frac{\varepsilon_1\varepsilon_2}{\varepsilon_1+\varepsilon_2}} \tag{2.21}$$

Solving for $\lambda$ at normal incidence yields an expression for the wavelength of surface plas-

mon modes

$$\lambda_{max} = a_0(i^2 + j^2)^{-1/2}\left(\frac{\varepsilon_1\varepsilon_2}{\varepsilon_1 + \varepsilon_2}\right)^{1/2} \tag{2.22}$$

Equation (2.22) predicts the surface plasmon modes excited when light of a given wavelength, $\lambda$ and direction $\theta$ is incident on a two-dimensional grating with a given lattice spacing.

In a similar approach to finding eq. (2.22), we can find the wavelength of Wood's anomaly, which explains the minima in the transmission spectra that occur on the lower wavelength side of each transmission peak (Fig. 1.1). The incident light is diffracted by the grating, and propagates in the dielectric. When the diffracted wave is tangent to the grating, and the wavelength matches the periodicity of the grating

$$\vec{k}_{diff} = i\vec{G}_x + j\vec{G}_y, \tag{2.23}$$

we have the condition for Wood's anomaly [4]. This is similar to eq. (2.20), except the waves are propagating in the dielectric, and are not bound to the electrons on the surface. The wavevector of this diffracted beam is given by [4]

$$k_{diff} = \frac{\omega}{c}\sqrt{\varepsilon_1}, \tag{2.24}$$

where $\varepsilon$ is the dielectric function of the propagation medium. $\varepsilon_1 = \varepsilon_{air}$ for waves scattered at the air-gold interface, and $\varepsilon_1 = \varepsilon_{glass}$ for waves scattered at the glass-gold interface, since we are talking about E-M waves in the dielectric. Combining equations (2.23) and (2.24), and using $\frac{\omega}{c} = \frac{2\pi}{\lambda}$ results in

$$\lambda_{diff} = a_0(i^2 + j^2)^{-1/2}(\varepsilon_1)^{1/2} \tag{2.25}$$

Equations (2.25) and (2.22) are very similar in form, the only difference being that the Wood's anomaly is independent of the metal's dielectric function, as the grazing diffracted order propagates in the dielectric, parallel to the surface. For a metal-dielectric interface, we have $\varepsilon_1 = \varepsilon_{air} > 0$ and $\varepsilon_2 = \varepsilon_{metal} < 0$, which gives

$$\frac{\varepsilon_1\varepsilon_2}{\varepsilon_1 + \varepsilon_2} > \varepsilon_1. \tag{2.26}$$

This results in the Wood's anomaly always occurring at a smaller wavelength than the Surface Plasmon mode (eqs. 2.25 and 2.22)

Another common method for exciting surface plasmons involves changing the dielectric in contact with the metal. If the dielectric constant is large enough, it will lower the light line in Fig. 2.3, such that it crosses the dispersion curve of the surface plasmons. This allows the photons to interact with surface plasmons while still conserving momentum. This technique is known as Attenuated Total Reflection (ATR), and the geometry of the technique is shown in Fig. 2.4.

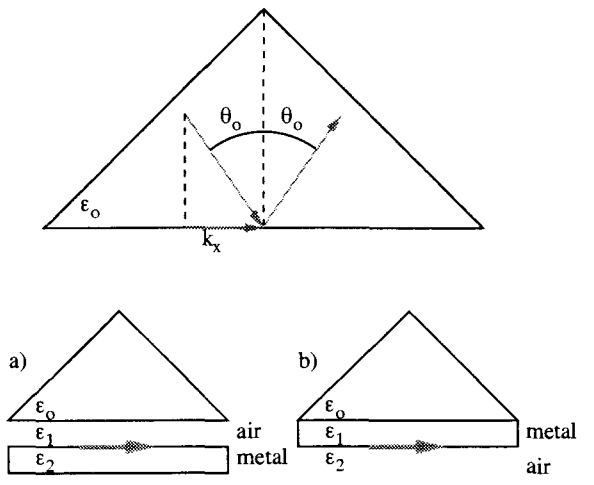


Figure 2.4: Schematic diagram of an ATR. a) The Otto configuration; a dielectric gap is present between the prism and the metal. b) The Kretschmann-Raether Configuration; the prism is in direct contact with the metal film [17].

### 2.2.3 Fresnel Coefficients

Fresnel coefficients provide insight into the origin and nature of surface plasmons from an optical perspective [18]. The Fresnel coefficients $r_p, r_s, t_p, t_s$ are related to the reflectivity, R, and transmissivity, T, of TM (Transverse Magnetic) and TE (Transverse Electric) modes of light. Neglecting any absorption, we can write R and T in terms of the Fresnel coefficients as [17]

$$\begin{aligned} R_{TM} &= r_p^2 \quad , \qquad R_{TE} = r_s^2 \\ T_{TM} &= t_p^2 \quad , \qquad T_{TE} = t_s^2 \end{aligned} \tag{2.27}$$

The Fresnel coefficient at normal incidence for reflection from an interface of two materials $i$ and $k$ can be expressed in terms of the material parameters [17]

$$r_{ik}^{p} = \left(\frac{k_{zi}}{\varepsilon_i} - \frac{k_{zk}}{\varepsilon_k}\right) \Big/ \left(\frac{k_{zi}}{\varepsilon_i} + \frac{k_{zk}}{\varepsilon_k}\right) \tag{2.28}$$

It is interesting to note that when the denominator of $r_p$ goes to zero,

$$\frac{k_{zi}}{\varepsilon_i} + \frac{k_{zk}}{\varepsilon_k} = 0, \tag{2.29}$$

we recover the dispersion equation for surface plasmons (2.14). The physical interpretation of the diverging Fresnel coefficient is not immediately evident. However, if we apply eq. (2.16), we can write the dispersion equation as

$$\frac{\varepsilon_i k_0^2 - k_x^2}{\varepsilon i^2} = \frac{\varepsilon_k k_0^2 - k_x^2}{\varepsilon k^2}, \tag{2.30}$$

where we have used $k_0 = \omega/c$, the wavevector of the incident wave. Solving for $k_x/k_0$ gives

$$\frac{k_x}{k_0} = \sqrt{\frac{\varepsilon_i \varepsilon_k}{\varepsilon_i + \varepsilon_k}}. \tag{2.31}$$

Consider an air-metal interface, in which case $\varepsilon_i \approx 1$ and $|\varepsilon_k| \gg 1$, and equation (2.31) becomes

$$\frac{k_x}{k_0} \approx 1. \tag{2.32}$$

This equality describes waves propagating in the $x$-direction, and are called evanescent waves. Thus if evanescent waves are present, the Fresnel coefficient will diverge according to the above argument. And since the Fresnel coefficient goes to infinity, a very small p-polarized evanescent wave can excite a large plane wave in the metal [18]. This large plane wave is a surface plasmon. The evanescent waves originate when an incident wave diffracts from a grating, since not only are diffracted orders excited, but non-propagating evanescent waves near the surface are also excited [18].

The Fresnel coefficients are also used to determine the reflection and transmission coefficients of a continuous metal film of thickness $d$, in an asymmetric environment:

$$\begin{aligned} R &= \left| \frac{r_{01}^{p} + r_{01}^{p} exp(2ik_{z1}d)}{1 + r_{01}^{p} r_{12}^{p} exp(2ik_{z1}d)} \right|^2 \\ T &= {t_{012}^{p}}^2 = \left| \frac{t_{01}^{p} t_{12}^{p} exp(ik_{z1}d_1)}{1 + r_{01}^{p} r_{12}^{p} exp(ik_{z1}d_1)} \right|^2 \end{aligned} \tag{2.33}$$

The power reflected from a rough metal surface is then [17]

$$P = \frac{1}{I_0}\frac{dI}{d\Omega} = \frac{1}{4}\left(\frac{\omega}{c}\right)^4 \sqrt{\varepsilon_0}\frac{|W(\theta)|^2}{\cos\theta_0}|t_{012}^P|^2|s(\Delta k_x)|^2 \tag{2.34}$$

where $t_{012}^P$ is defined above, $|W(\theta)|^2$ is the dipole function, and $|s(\Delta k_x)|^2$ is the Fourier transform of the roughness correlation function. This equation, which relates the reflected power to the roughness of the surface via the Fourier transform of the surface, motivates the idea that the transmission and reflection from a surface involving surface plasmons is related to the Fourier transform of the surface.

### 2.2.4 A 3D Theory

Ebbesen et. al. present a fully three-dimensional model of the enhancement effect. A matrix equation successfully predicts the location and relative amplitude of the peaks [7], and when simplified, is of the form of the transmissivity predicted by the Fresnel co-efficients (eq. (2.33)). In the simplified version of this theory, the transmissivity is given by

$$t_{00} = \frac{\tau_{01}^{12} e^{-|q_{z1}|h}\,\tau_{10}^{23}}{1-\rho^2 e^{-2|q_{z1}|h}}, \tag{2.35}$$

where we have

$$\tau_{01}^{12} = 2S_0/(G_2+G_1), \quad \tau_{10}^{23} = 2G_2/(G_2+G_1), \quad \rho = (G_2-G_1)(G_2+G_1), \quad \text{and}$$

$G_1$ and $G_2$ are conductances in region 1 and 2. For a hole array in a perfect conductor, they are given by

$$G_1 = q_{z1}/g, \qquad G_2 = S_0^2 + 2S_1^2 g/k_{z1}$$

and finally, where

$$g = \omega/c, \quad S_0 = d/L, \quad S_1 = S_0 sin[k_{x1}d/2]/(k_{x1}d/2), \quad k_{z1} = \sqrt{g^2 - k_{x1}^2}$$

Wood's anomaly comes out of this model as a zero in either $\tau_{01}^{12}$ or $\tau_{10}^{23}$. This is when the conductance in medium 1 or 3 is infinite.

In this equation, we have $\tau_{01}^{12}$ and $\tau_{10}^{23}$ bringing modes in and out of the film, taking into account the mismatch in impedances across the interface. The $e^{-|q_{z1}|h}$ term propagates the

modes through the film. While this theory is excellent at predicting the peaks in the transmission intensity, it assumes square nanoholes, as the authors state that the transmission is independent of the hole shape. This makes the theory impractical to apply to the study of the dependence of the transmission enhancement on the nanohole shape.

# Chapter 3

# STM Experiment

## 3.1 STM Light Emission

The design and testing of an STM modified to collect tunneling induced light emission (STM-LE), is outlined below. The STM that was modified is a commercial Omicron STM-1. It operates at atmospheric pressure and room temperature but has the necessary hardware to be fitted to a UHV chamber. The STM was previously altered with a homemade Ballistic Electron Emission Microscope (BEEM) modification [19]. BEEM provides a nanoscale probe for the barrier height of a Schottky interface or other heterojunctions.

The STM was modified to collect light emitted in various tunneling processes. Whether this is light emitted from Surface Plasmon excitation and decay, or light emitted from electron-hole recombination in semiconductor nanostructures, the light collection experiment can be broken down into three distinct stages:

1. Collection of light emitted.
2. Conversion of the information of a light pulse into an electrical signal.
3. Correlation of the electrical signal with the simultaneously collected STM or BEEM data.

One method used to realize the first stage, the collection of the light emitted, involves locating the STM tip at the focal point of an elliptical mirror [14]. In this way a significant portion of the light emitted at the point of tunneling can be collected and measured at the

second focal point of the elliptical mirror. However, the physical constraints on the STM required to realize the placement of the elliptical mirror, generally require the fabrication of a new STM, with this design constraint in mind. Another approach, the one attempted in this thesis, involves the placement of a fiber-optic waveguide in proximity to the STM tip. The light collected will then be directed to a photodetector by the fiber optic.

The photodetector is the second stage in the apparatus and converts the optical signal into an electrical current pulse. The electrical current is in turn converted into a voltage signal, and fed into the STM control box, to be collected simultaneously with the STM and/or BEEM data, the third stage in the process.

### 3.1.1 Optics for Light Detection

The light emitted by an STM (STM-LE) must be collected and transported to the detection apparatus. If we consider the light emitted in the STM as a point source, we can consider whether it is more efficient to collect the light using a fiber optic, positioned as close as possible to the light source, or whether use of lenses would improve the collection efficiency. In the following discussion, a multimode fiber from Thorlabs [20] is assumed. The assumed fiber has a Numerical Aperture $NA = 0.48$, a core diameter of 1.0 mm and a cladding and buffer diameter of 1.4 mm. The core of a fiber optic is where the light propagates through the fiber, the cladding provides the step in the index of refraction, and the buffer is the outer layer of the fiber.

### 3.1.2 Butt Coupling a Fiber

The easiest solution is to butt couple the fiber optic to the point source of light. As seen in Fig. 3.1 the distance of closest approach, $s_0$ is determined by the total diameter of the fiber, the buffer diameter.

$$\tan(45°) = \frac{D_{buffer}}{2s_0} \quad \Rightarrow \quad s_0 = \frac{D_{buffer}}{2} \tag{3.1}$$

We can then determine the angle, $\theta$, subtended by the core of the fiber when positioned at the distance of closest approach.

$$\tan(\theta) = \frac{D_{core}}{2s_o} = \frac{D_{core}}{D_{buffer}} \tag{3.2}$$

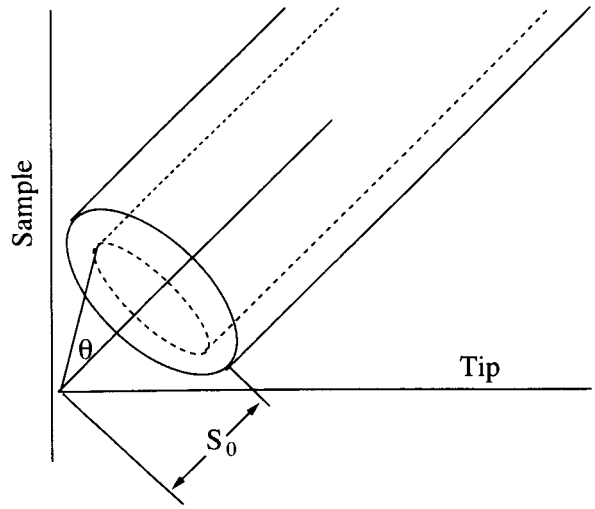


Figure 3.1: The fiber butt-coupled to the source.

For our fiber we have $D_{buffer} = 1.4 D_{core}$, which gives $\theta = 35°$.

The *NA* of the fiber is related to the indices of refraction of the fiber core and the fiber cladding, and is fixed for a given fiber. The largest angle possible where the fiber still collects the light, is determined by the numerical aperture *NA* of the fiber.

$$\sin(\theta) = NA \tag{3.3}$$

For our fiber, NA=0.48, which gives an angle of 28.6°. This angle is smaller than the angle subtended by the core of the fiber, indicating we are limited by the numerical aperture of the fiber, not the geometry of the setup.

The solid angle of the light collected is found by using the expression which relates the two-dimensional azimuthal angle $\phi$ of a cone to the solid angle spanned by the cone

$$\Omega = 2\pi\big(1 - \cos(\phi)\big) \tag{3.4}$$

where for Fig. 3.1 $\phi = 2\theta$. This gives us a solid angle of $\Omega = 2.88$.

### 3.1.3 Using a Pickup Lens

A lens may be used to improve the solid angle of the light collected. Consider the geometry in Figure 3.2, where for a lens of diameter D, we obtain the definitions of the angles $\alpha$ and

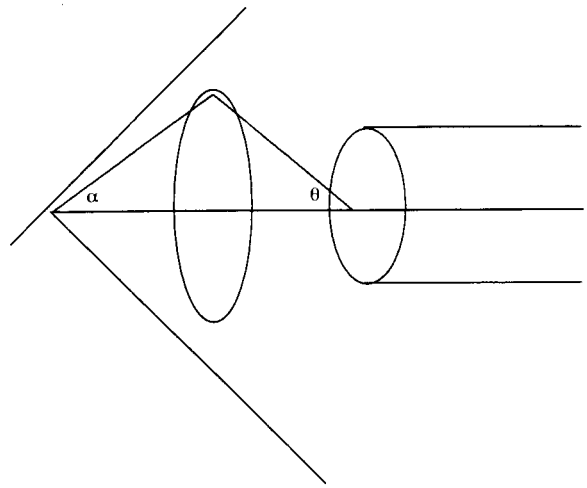


Figure 3.2: The fiber coupled to the source with a lens

θ.

$$\tan(\alpha) = \frac{D}{2s_o} \qquad \tan(\theta) = \frac{D}{2s_i}. \tag{3.5}$$

The source distance $s_o$ and image distance $s_i$ are related to the focal length $f$ by the thin lens formula

$$\frac{1}{f} = \frac{1}{s_o} + \frac{1}{s_i}. \tag{3.6}$$

The $f/\#$ of the lens is defined as

$$f/\# = \frac{f}{D}. \tag{3.7}$$

Equation (3.7) allows us to rewrite the thin lens formula in terms of the angles in Figure 3.2, such that

$$\frac{1}{f/\#} = 2\tan(\alpha) + 2\tan(\theta). \tag{3.8}$$

We again can consider the physical limit, where the lens is as close to the point source as possible. In this case, we have the upper limit of $\alpha$ of 45°, and the upper bound on $\theta$ as defined by eq. (3.3). This gives a lower bound on the f-stop of f/# = 0.323, and an upper bound on the solid angle of 6.28 steradians.

Thus, we have a practical limit on the solid angle of light collected by our optical system of 6.28 steradians. To put this in perspective, Schlittler et al. successfully detected an STM-LE signal with solid angles of both 0.04 and 0.1 steradians [14], [21].

### 3.1.4 Alternative Lenses Available

Aside from the traditional lens mentioned, there are additional types of lenses that can be considered, such as GRadient INdex (GRIN) lenses, and spherical lenses. These alternative lens types have the advantage that they can be mounted directly onto the end of the fiber, making alignment a much simpler process.

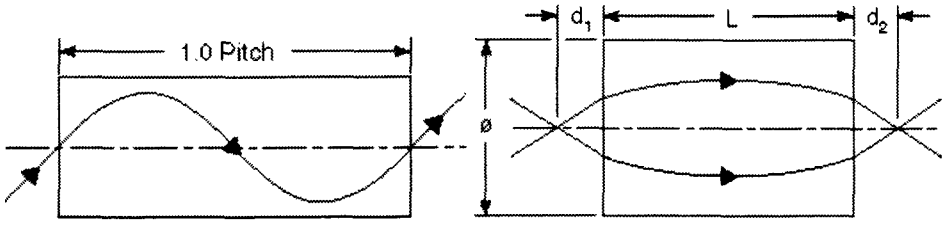


Figure 3.3: a) A GRIN lens with pitch 1, and b) a GRIN lens with pitch 0.29 [22]

Grin lenses are cylindrical lenses that have a index of refraction graded radially. They are characterized by their pitch, which indicates what portion of a sinusoidal path the light ray would follow if it traversed the lens. A GRIN lens with pitch 1.0 is shown in Figure 3.3a. A pitch 1.0 grin lens has a light ray leave it at the same angle it entered the lens. A grin lens of pitch 0.29 is more applicable, see Figure 3.3b. However, grin lenses are very wavelength specific, and the numerical aperture of a grin lens is similar to that of a fiber optic. Thus they are not the ideal lens for the situation.

Spherical lenses can be attached to the end of the fiber optic cable, as is the case for GRIN lenses. A 1 mm diameter spherical ball lenses has an f-stop of $f/\# = 0.69$ [22], which meets our requirements, and is an ideal candidate for increasing the amount of light collected from the STM.

### 3.1.5 From Photons to Electrons

The first detector tried was a Hamamatsu R928 photo-multiplier tube (PMT), with a spectral range of 185 nm - 900 nm, and a dark current of 3 nA. The PMT emits a current pulse which has to first be amplified and conditioned in order to be counted. The electronics used

to perform this conditioning are described below.

### 3.1.6 Current to Voltage Conversion

There are two stages to the electrical conditioning of the current pulse that is emitted by the photo-multiplier tube. First the current pulse has to be converted to a voltage pulse, to allow further manipulation. This is achieved using a fast inverting amplifier. An OPA688 Unity Gain, Stable Wideband Voltage Limiting Amplifier has a response time sufficient for this application (Fig. 3.4). At the next stage, a high speed differential amplifier discriminates pulses below a variable voltage level. This stage is necessary to exclude noise pulses that occur when electrons are spontaneously emitted from the various dynodes of the photo-multiplier. The output from the discriminator is then sent to a TTL pulse shaper, which conditions the voltage pulse within TTL voltage levels, and a minimum time duration. Fortunately the TL3016 Ultra Fast Low Power Precision Comparator was able to swing from 0 to 5 Volts in the short duration of the pulse, within TTL Voltage requirements, thereby simultaneously filling the role of discriminator and TTL pulse shaper. After these

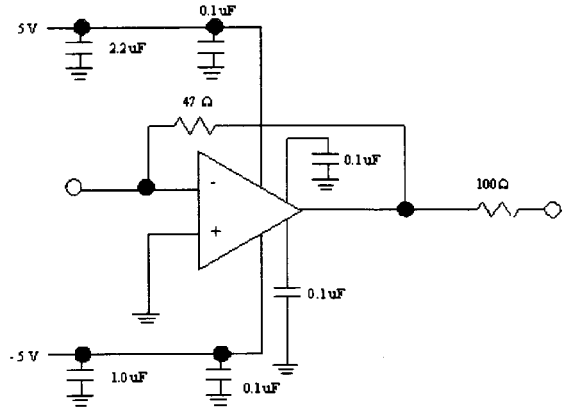


Figure 3.4: STM-LE preamp circuit - OPA688 Unity Gain, Stable Wideband Voltage Limiting Amplifier

two stages of electrical conditioning, the pulses are counted, and the count rate is fed into the STM control unit as an analog signal, proportional to the count rate.

## 3.2 Results

Initial experiments with the STM-LE setup indicated that the dark count was too high, and any potential signal was being swamped. Thus, in order to improve the response of the photodetector, the dark count needed to be reduced. This was achieved by cooling the photo-multiplier to -10°C, which reduces the thermal-emission of electrons from the PMT's photocathode. Additionally, the STM chamber was light-proofed, with increasing refinement. Once the minimum dark count was achieved, the correct discriminator voltage setting was determined by measuring the dark current of the PMT as a function of the discriminator voltage, and comparing the dark current measurement to the one carried out when a LED light source was introduced to the STM chamber. These results are shown in Figure 3.5, where we can see that both the dark current, and the LED signal count decrease with increasing discriminator voltage until $V \sim 0.07$ volts, where both signals are quenched by the discriminator. The current measurement was uncalibrated, as it was the inflection point at 0.07 Volts that was sought after, not the magnitude of the dark current.

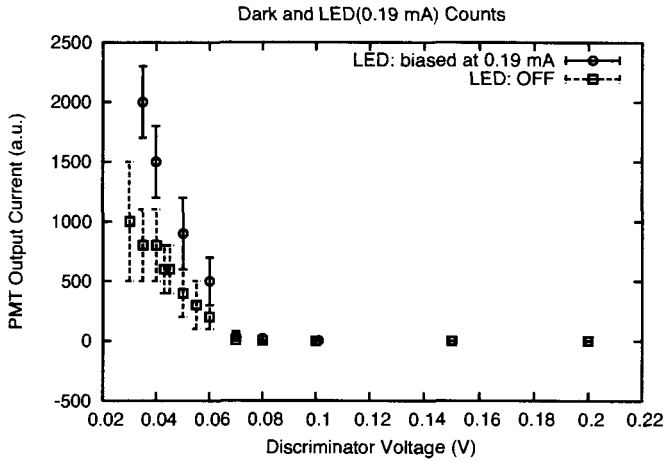


Figure 3.5: Dark Current of Hamamatsu R928 PMT.

Ultimately, the Hamamatsu PMT did not perform adequately, and a new photodetector was tried. A Perkin Elmer C982 Channel Photo-multiplier (CPM) offers many advantages over conventional photo multiplier tubes. This includes a dark current of 25 pA, two orders of magnitude lower than the Hamamatsu PMT, and a current gain 5 times larger. With a

smaller spectral range of 165-650 nm, a dark count of 3 cps is achievable, without cooling. Additionally, the Perkin Elmer photon counting module replaces all the homemade electronics described above, as it has internal electronics that convert the photon signal to TTL output. It has a fiber connector pre-mounted, and cooling the CPM will not improve its performance. Therefore, the CPM can be mounted much closer to the STM, requiring a shorter fiber optic cable, and hence less fiber loss.

With the new photodetector, samples of thermally evaporated Au were scanned using PtIr stm tips fabricated by cutting with a razor blade. The tip bias applied was between 0.5 - 3 eV. The gold showed atomic terraces in the STM image, but no light emission was detected. It became evident that the tip radius was too large, and the mechanism used to position the fiber optic above the STM tip was insufficient.

It has been shown that the efficiency of the STM-LE process increases with decreasing tip radius, for $\rho > 80$ nm [23](see Fig. 3.6). This effect can be interpreted as the tip shadowing the light emission, and hence decreasing the emission efficiency. For tips of radius smaller than $\rho < 30$ nm the emission efficiency is predicted to increase with increasing tip radius. At this size scale the tip radiation efficiency increases with size, since a larger antenna puts out more power. The optimal tip radius is then believed to be on the order of $\sim 50$ nm.

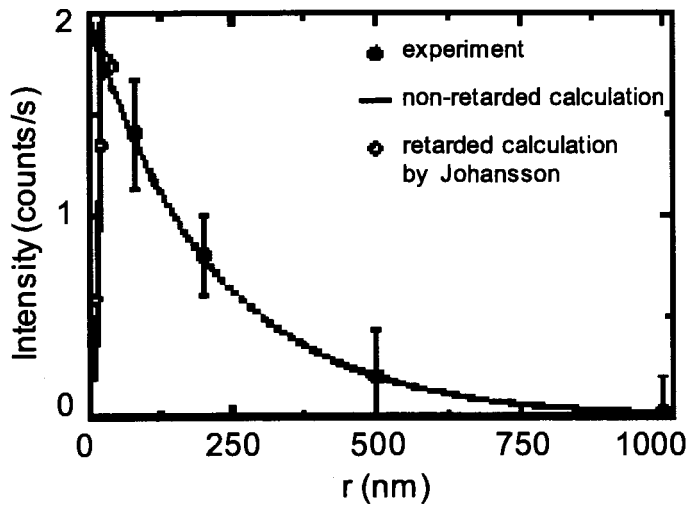


Figure 3.6: STM-LE intensity vs. tip radius [23].

As a result, electrochemical etching of the Pt-Ir(90:10) tips used in the experiment was tried, in order to improve the efficiency of the STM-LE. The conventional method of cutting the tips with a razor blade results in a tip curvature with too large a radius of curvature.

The apparatus used to etch the tips is shown in Figure 3.7. It consists of a $CaCl_2/H_2O$/acetone electrolyte, where 7 g of $CaCl_2$ is dissolved in 40 mL of acetone saturated $H_2O$. The submerged Pt-Ir wire is covered in silicone (a bead of RTV silicone 5 mm in diameter and 1 cm long). A gap is opened up in the silicone, where the electrochemical etching is to take place. A 10 V AC signal is applied between the tip and a carbon electrode, and once the Pt-It etches all the way through, the tip falls off into a "tip-catcher" placed beneath the Pt-Ir wire [24].

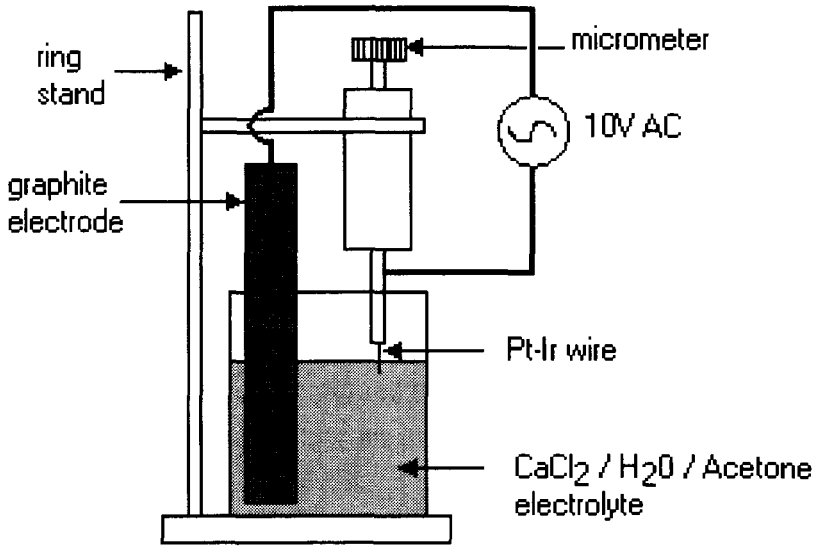


Figure 3.7: The apparatus used to electrochemically etch Pt-Ir STM tips [24].

Some typical Pt-Ir etched tips are shown in Figure 3.8. A thick carbon deposit is left on the STM tip after the electrochemical etch, however it is easily removed by placing the tip in an ultrasonic bath for several seconds. Tip radii on the order of 500 nm are easily achievable, but the process needs to be further refined to try and get closer to the optimal tip radius of curvature value of 50 nm.

To overcome the problem with positioning the fiber optic, a new mechanism was designed using set screws backed with springs to position the fiber optic. However, given

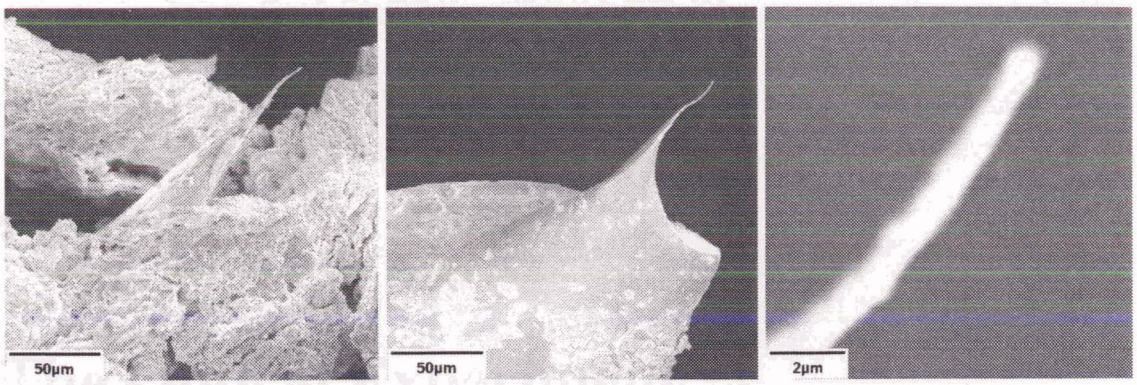


(a) (b) (c)

Figure 3.8: SEM images of PtIr STM tips, a) after etch b) after ultrasonic cleaning, c) at higher magnification

the long lever holding the fiber optic, the positioning technique was very susceptible to vibration and friction, which made the alignment next to impossible. The variability in the position of the tip is on the order of the diameter of the tip. A new technique needs to be devised, where the fiber optic is mounted to the STM tip holder, and coupled optically to the photodetector. This would allow an immediate alignment of the fiber optic with the STM tip.

# Chapter 4

# The Optical Experiment

## 4.1 The Experimental Arrays

A series of experiments was planned to explore the effect of the hole shape, and the type of basis, on the transmission enhancement of nanohole arrays. The spacing of an array of nanoholes determines the wavelength of the surface plasmon enhanced transmission. The detector used in the transmission measurements was limited to a wavelength range of 500 nm - 1100 nm. Therefore, the array spacing of 710 nm was chosen to produce transmission in this range. From equation (2.22) we can then predict the wavelength of various surface plasmon resonances.

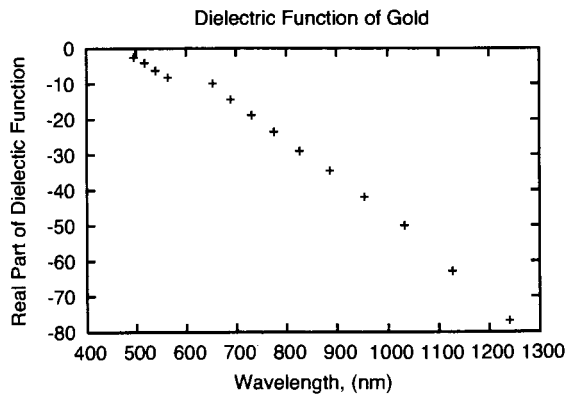


Figure 4.1: The Dielectric Function of Gold [25]

The dielectric function of Au varies strongly with the wavelength (Fig. 4.1). In order to calculate the plasmon modes, a value of $\varepsilon_{Au} = -20$, was initially chosen, along with $\varepsilon_{air} = 1$, $\varepsilon_{glass} = 2.1$ [25]. Once initial wavelengths of the surface plasmon modes were determined, $\varepsilon_{Au}$ was re-evaluated for each wavelength using Fig. 4.1. In this way, the surface plasmon mode was determined recursively, taking into account the strongly varying dielectric function of gold in the wavelength range of interest. This gives a (1,0) surface plasmon mode at a wavelength of 730 nm for the air-gold interface. At the glass-gold interface, the (1,0) mode would be located at a wavelength of 1050 nm, at the limit of the range of the detector. Also, the (1,1) glass-gold mode at 760 nm is close in value to the (1,0) air gold mode at 730 nm. This is a result of the material choice; a different metal and/or dielectric will not necessarily have the same modes overlap. Various surface plasmon resonances are tabulated in Figure 4.1, along with the wavelength of the Wood's anomaly predicted from equation (2.25)

| Surface Plasmon | Wavelength (nm) | | Wood's Anomaly (nm) | |
|---|---|---|---|---|
| Resonance | Air-Gold | Glass-Gold | Air | Glass |
| (1,0), (0,1) | 730 | 1050 | 710 | 1050 |
| (1,1) | 550 | 760 | 500 | 740 |
| (2,0), (0,2) | - | 590 | 360 | 530 |
| (2,1), (1,2) | - | 530 | 320 | 470 |

Table 4.1: Calculated wavelengths for various surface plasmon modes and Wood's Anomalies for a thin Au film, with holes spaced 710 nm apart.

With the chosen spacing in hand, two series of elliptical nanohole arrays were created to probe the asymmetric properties of the surface plasmon generation, propagation and decay. The first series consisted of arrays of elliptical nanoholes with varying aspect ratio, where the aspect ratio is the ratio of the minor axis of the ellipse to the major axis of the ellipse. Arrays of elliptical nanoholes with an aspect ratio 0.3, 0.5, 0.6, and 0.9 were created.

In the second series, the angle of orientation of the ellipses in the array was varied (see Fig. 5.2). The angle of orientation is the angle between the major axis of the ellipse, and the x-axis of the array. The aspect ratio was then held constant at 0.5, and the angle of

orientation of the ellipse was rotated from 0°to 45°in 15°increments.

Furthermore, arrays with a two hole basis were created, to investigate the effect of the basis on the transmission through the array. The basis consisted of two holes of radius R, with a center-to-center displacement constant in the y-direction, $\Delta Y = 3R$, and a varied displacement in the x-direction, $\Delta X = 0R, 1R, 2R, 3R$.

## 4.2 Nanohole Array Fabrication

Arrays of nanoholes were milled into a 100 nm gold film on a glass substrate, with a 5 nm layer of chromium between the gold and glass for better adhesion. The holes were milled using the Focused Ion Beam (FIB) of a FEI Dual beam Strata 235 Field-Emission Scanning Electron Microscope (SEM). The 30 kV Ga ion beam has a 7 nm minimum spot size.

### 4.2.1 FEI Pattern Files

The FIB software provides a CAD-like user interface for defining milling patterns. By selecting predefined shapes such as circles, squares, rectangles, etc., one can draw out the desired pattern on the e-beam or ion beam image, and the FIB will mill that pattern. These patterns can be saved as text files, so it was a logical step to write a program to generate these pattern files, to mill arrays of circles. However, there are some significant drawbacks to this pattern file technique. For instance, one is limited to the set of predefined shapes, which omits certain basic shapes, such as ellipses. Additionally, the number of distinct objects in the pattern is limited.

### 4.2.2 Low-Level Stream Files

The software provides a "lower level" patterning technique by allowing direct access to the patterning data acquisition board (DAQ) of the FIB using a "stream" file. It is a 12-bit DAQ, so there are $2^{12} \times 2^{12}$, or $(4096 \times 4096)$ pixels we can access [26]. However, while this DAQ is 12-bit, we cannot access all 16 million co-ordinates in a single pattern. Due to memory restrictions of the DAQ board, only 1 million can be accessed at a time. The format of the "stream" file is described in Fig. 4.2. The first line of the file consists of an

**line 1** s; the file begins with an s (indicating a stream file),

**line 2** #; the number of loops (1 = serial)

**line 3** N; the total number of coordinates

**line n** dwell time, x coordinate, y coordinate

Figure 4.2: The format of the "stream" file [26].

"s", indicating the file is a stream file. the second line is the number of times the pattern is to be repeated, and the third line is the total number of co-ordinates to be milled. Following the first three lines, there is one line for each $(X,Y)$ coordinate, beginning with the dwell time (in nanoseconds) followed by the x and y coordinate. An example of a stream file is shown in Fig. 4.3. The algorithm used to create a stream file that will mill a grid is

```
s
1
4
2000 0 0
2000 4095 0
2000 0 4095
2000 4095 4095
```

Figure 4.3: Example stream file, with 4 co-ordinates, one at each corner of the DAQ board.

quite straightforward. First, the basis of the lattice, such as an ellipse, is created in a small data structure. This basis can then be translated to each of the lattice points. The number of points (line 3 of the stream file) is then just the number of points in the basis times the number of lattice points. This value and the individual data points can then be written directly to a file.

If one wants to superpose two arrays of different lattice spacing, care must be taken with respect to overlapping holes. Overlapping data points should be avoided, as we only have 1 million data points to work with at a time, and the ion beam should not visit the same co-ordinate twice. By storing the coordinates before they are created, one can check for duplication of data points, before writing to the stream file. The number of co-ordinates also has to be counted, and output in the third line of the file. Depending on the language one is using to write the stream file, care must be taken in choosing the data type to store the co-ordinates. For instance, a 16 million element array is overkill when we are limited to 1 million data points. In the Python scripting language (see Appendix A.1) a hash table or (dictionary) can be used to store the data. Each coordinate stored uses three bytes, two for the hash key, the $(x,y)$ co-ordinates, and one byte for the hash value.

The 1 million coordinate limitation causes problems when trying to make a large, densely packed array. This limitation can be overcome by staggering the mill points. For instance, when defining the basis, one can skip any point where the point to it's left is defined. Then, if the dwell time at that point is increased, or the ion current is increased, the pattern will still be milled through.

### 4.2.3 Creating Stream Files

The program stream.py (see Appendix A.1) creates stream files for grids with elliptical holes. It can create arrays with a single or double hole basis, and can superimpose two arrays of different lattice spacing. The help screen output of the program, when it is called with no arguments, is shown in Fig. 4.4. If the program is called with a single argument and no options, the single argument is taken as the output filename, and a stream file is created with the default values, which are circular holes 10 pixels in diameter, and 75 pixels apart. Each of the program's options provide a way of varying the parameter space of the stream files, away from these default values.

For example, running the command:

```
stream_ellipse.py -x12 -y12 -s100 -q100 -n2 -u0 -v36 -d300 stream.str
```

creates a stream file for a grid with two arrays offset from one another 0 pixels in the x-direction, and 36 pixels in the y-direction, and a dwell time of 300 ns. Alternatively, if

```
bleathem@boron: /Lab/Uvic/Patterns/stream_bin$ ./stream_ellipse.py
usage: stream_ellipse.py [OPTIONS] FILE

options:
-h, –help              show this help message and exit
-xXA, –x-axis=XA       The length of the x-axis of the ellipse. Default=10
-yYA, –y-axis=YA       The length of the y-axis of the ellipse. Default=10
-sS, –spacing=S        The spacing of the ellipses. Default=75
-qQ, –spacing2=Q       The spacing of the 2nd array of ellipses. Default=75
-dD, –dwelltime=D      Dwell time of the ion beam. Default=100
-aA, –angle=A          Angle of rotation of the ellipse(degrees). Default=0
-lL, –loops=L          The number of times to repeat the pattern. Default=1
-nN, –num=N            The number of shapes in the basis, 1 or 2. Default=1
-uXO, –xoffset=XO      The x-offset of the second shape in the basis.
                       Default=15
-vYO, –yoffset=YO      The y-offset of the second shape in the basis.
                       Default=15
```

Figure 4.4: Default stream_ellipse.py output

one uses the windows compiled version of the program on the FEI computer, the ".py" file extension is replaced by a ".exe" file extension.

### 4.2.4 FEI's PATTERNS Program

The FEI people have provided a program "PATTERNS.exe" that is used to convert bitmap files into stream files. This program crashes when used to create large stream files, so this feature was not used. It is however useful to preview what a stream file will look like, and whether it is a valid stream file (it will not load if it is invalid).

### 4.2.5 Etching Results

The stream file created with the above command created holes 170 nm in diameter, and spaced 710 nm apart. So we conclude that at the working magnification, 5000x, that one pixel corresponds to 7.1 nm per pixel. The holes that were milled with ion currents of 100 pA and 300 pA yielded similar results for appropriate dwell times. A calibration pattern was created to measure the rate at which the ion beam mills. A series of lines with dwell time increasing from 0 to 600 ns were milled. An SEM image (Fig. 4.5) then allows one to determine at what dwell time the beam mills through the gold.

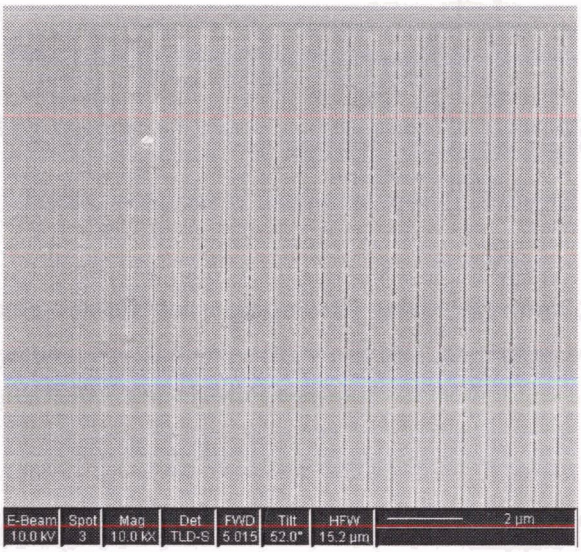


Figure 4.5: SEM image showing a series of lines fabricated with dwell times varying from 0 to 600 ns in 15 ns increments, with an ion current of 300 pA.

## 4.3 Transmission Spectra Collection

A schematic of the experiment used to measure the transmission spectra of the nanoholes in gold is shown in Fig. 4.6. The apparatus used was set up at the University of Victoria, and was used by both myself and collaborators [27,28]. The light from the source is collimated by a pair of lenses. This beam of light is then focused down to a spot by a microscope

objective lens. Thus the light is incident on the sample from a range of angles. According to eq. 2.21, the surface plasmon mode excited varies with the angle of the incident light. The transmitted light is collected by an optical fiber, which directs the light to an Ocean Optics spectrometer. By adjusting the position of the fiber optic, these different plasmon modes can be investigated [3]. In this way, the fiber was positioned to measure the transmitted light associated with normal incident light. As mentioned, the spectrometer used has a wavelength range of 500 - 1100 nm. The arrays of nanoholes are observed through an optical microscope, which aids in positioning the sample for maximum transmission.

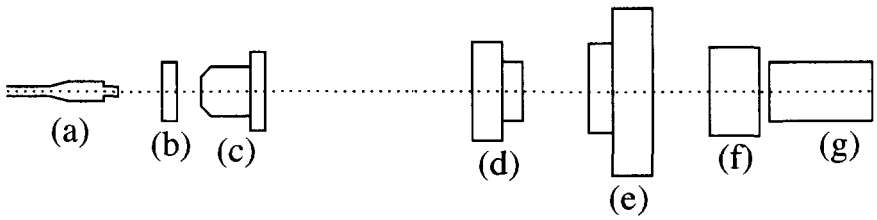


Figure 4.6: Nanohole transmission experimental setup. (a) Fiber optic. (b) Sample. (c) Microscope objective, 20x, 0,40 NA. (d) Weak lens. (e) Polarizer. (f) Camera lens. (g) White light source with a blackbody spectrum.

A spectrum was recorded of the transmission of light through each array of nanoholes. Over the wavelength range of the detector, peaks in the transmission were observed when the light coupled with a resonant surface plasmon mode. The transmittance spectra were background corrected and normalized to the intensity distribution of the light source. To this end, a background spectra was collected by measuring the transmission through the gold, away from the arrays of nanoholes. This background spectrum was subtracted from the sample spectra, to compensate for the transmission through the gold film (Fig. 4.7)

The intensity distribution of the white light source was also accounted for, (Fig. 4.7). To do this, a portion of the gold was scratched off the slide and a spectrum of the source collected through the glass slide only. The sample spectra was then normalized to this intensity distribution.

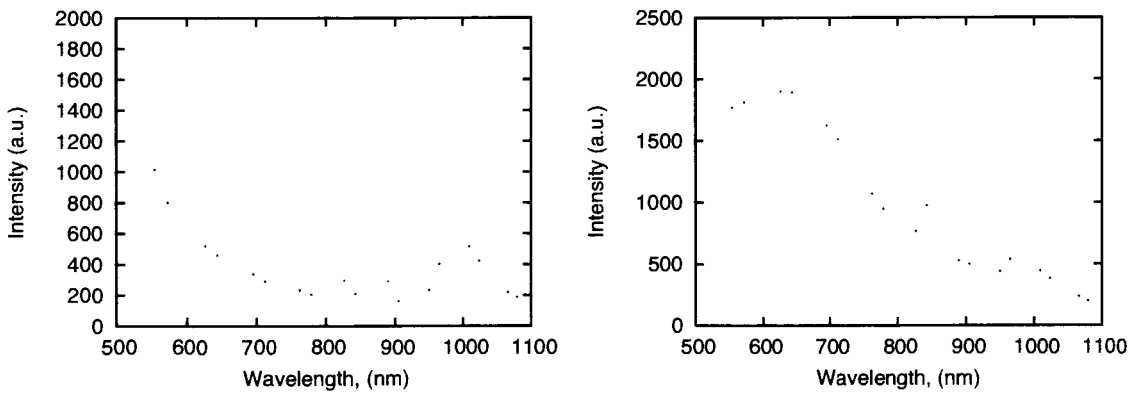


Figure 4.7: Transmission spectrum a) through the 100 nm gold film on glass, and b) through glass only. The spikes come from background illumination.

# Chapter 5

# Results

## 5.1 Ion Milling Results

The SEM images of two attempts to mill circular holes are shown in Figure 5.1. The pair of images demonstrate the importance of a correctly stigmatized ion beam. If the ion beam is astigmatic, the results of the milling are not as expected. Additionally, it was found that if the gold film was not adequately grounded, charging effects could cause a distortion of the shape.

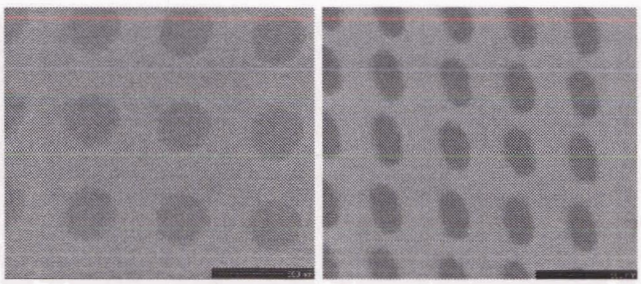

(a) (b)

Figure 5.1: SEM images of two attempts to mill circular nanoholes where a) the ion beem was correctly stigmatized and b) the ion beam was astigmatic. The scale line denotes a length of 500 nm.

The results of milling a series of ellipses is shown in Figure 5.2. The projected array spacing of 710 nm was achieved within an acceptable tolerance. In each of the arrays, the spacing was measured to be 715 ± 5 nm. The targeted hole size was 284 × 142 nm, and they are measured to be in the range 210 ± 10 × 100 ± 10 nm, 25% under milled. On average, the targeted angles fell within ± 3° of the targeted value, in each of the 4 arrays.

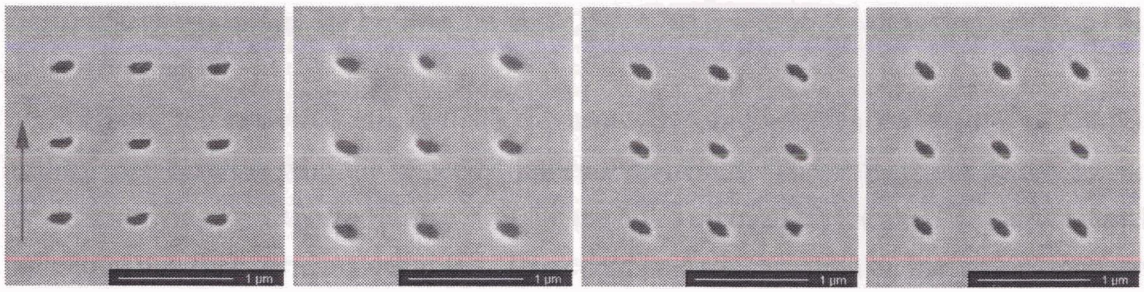

(a) $\Delta\theta = 0°$ (b) $\Delta\theta = 15°$ (c) $\Delta\theta = 30°$ (d) $\Delta\theta = 45°$

Figure 5.2: SEM pictures of elliptical nanoholes with a 1:2 aspect ratio, rotated at a) 0°, b) 15°, c) 30°, and d) 45°.

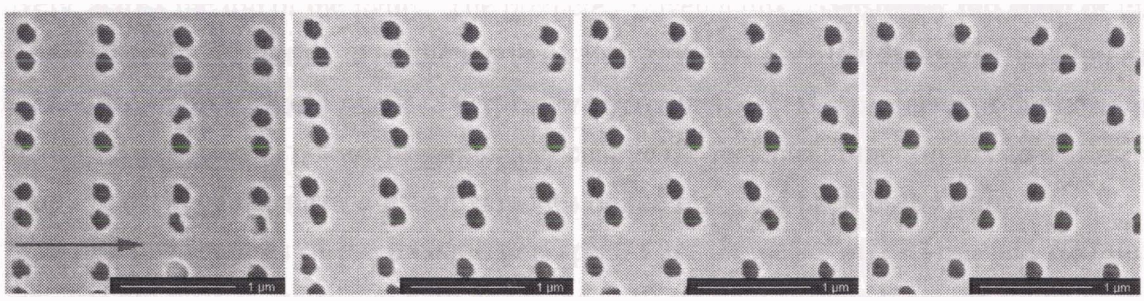

(a) $\Delta X = 0R$ (b) $\Delta X = 1R$ (c) $\Delta X = 2R$ (d) $\Delta X = 3R$

Figure 5.3: SEM pictures of "double hole" nanoholes, where the x-offset between the holes was incremented is steps of the radius, R. $\Delta R = 1R, 2R, 3R$.

Similarly, SEM images of the double holes are shown in Figure 5.3. For the double holes, the array spacing was also targeted to be 710 nm, and the spacing for all the arrays was measured to be in the range 710 ± 5 nm. The hole diameter was programmed to 170 nm, and was measured to be 150 ± 10 nm, close to the planned size. The planned values of the offset between the holes were 0, 80, 160, and 240 nm in the x-direction, and a constant 240 nm in the y-direction. The measured values of the offset were 0 ± 10, 100 ± 10, 160 ± 10, 250 ± 10 nm in the x-direction, and 250 ± 10 nm in the y-direction, close to the expected offsets.

For both the arrays of ellipses and the arrays of double holes the results of the ion milling give features with the expected lattice dimensions. The objects are at the correct locations, giving the expected lattice size, but the holes themselves are smaller than planned, indicating that they were under-milled. This could be corrected with an increased ion beam current, or an increased dwell time at each of the (x,y) coordinates.

## 5.2 Transmission Results

A typical transmission spectrum, for an array of ellipses with a spacing of 710 nm, is shown as the solid line in Figure 5.4. The wavelengths predicted in Table 4.1 for the surface-plasmon modes and the Wood's anomaly are marked with solid and dashed lines respectively, across the top of the figure. The predicted wavelengths consistently fall short of the observed peaks. However, in predicting the wavelengths we used the dielectric function for a smooth continuous gold film as a first-order approximation. The presence of the holes in the film is expected to not only significantly change the dielectric function but also allow a coupling between the surface-plasmon modes on the front and back of the film.

Some key features of the transmission spectra are the peaks at 790 nm and 620 nm. The 790 nm peak is associated with either the (1,0) air-gold surface-plasmon mode or the (1,1) glass-gold mode. The (1,1) Wood's anomaly prematurely truncates the 790 nm peak, which gives the impression that there is a 2nd small peak at 750 nm. This makes it difficult to determine whether the 790 nm peak is two peaks super-imposed, or two peaks side by side. For the same reason, it is difficult to associate the 620 nm peak with either the (2,0) glass-gold surface-plasmon mode or the (1,1) air-gold mode. To better identify the peaks, one would have to have a better idea of how the dielectric function of the metal is affected

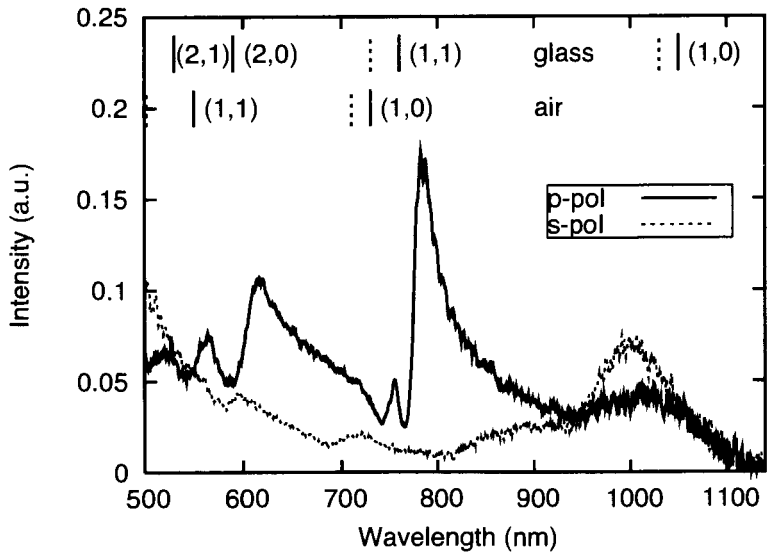


Figure 5.4: Transmission spectra for unrotated (0°) elliptical nanoholes. The solid line corresponds to the incident light perpendicular to the major axis of the ellipse (p-polarization), and the dashed line corresponds to the incident light parallel to the major axis of the ellipse (s-polarization). The calculated surface-plasmon modes are marked with solid lines, and those of the Wood's anomalies marked with dashed lines.

by the presence of the holes.

The transmission spectrum for an array of circular nanoholes is similar to the spectra shown as the solid line in Figure 5.4, independent of the polarization of the incident light. However, if the nanoholes are elliptical in shape, the spectrum changes with the polarization.

## 5.3 Polarization Effects

For elliptical nanoholes, irradiated with light polarized perpendicular to the major axis of the ellipse (p-polarized), a transmission spectra like the solid line in Figure 5.4 is observed. If the polarization is then rotated 90°, so that it is parallel to the major axis of the ellipse (s-polarized), a transmission spectra like the dotted line in Figure 5.4 is observed. The

enhancement effect then has a polarization dependence for arrays of anisotropic nanoholes.

### 5.3.1 Aspect Ratio of the Ellipses

A series of arrays with varying aspect ratio was created and measured by collaborators at Simon Fraser University, and the University of Victoria [2]. These results showed that the ratio of the transmitted intensity for p and s-polarized light depended on the aspect ratio of the ellipse [2]. The depolarization ratio is the ratio of s-polarized light to p-polarized light, and a plot of the depolarization ratio versus the aspect ratio of the holes is shown in Figure 5.5, where the solid line represents a quadratic fit to the data.

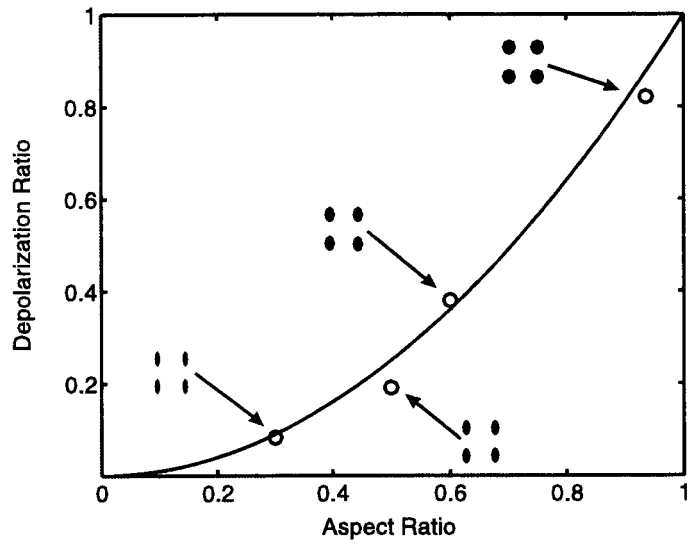


Figure 5.5: Depolarization ratio as a function of the hole aspect ratio [2].

### 5.3.2 Orientation of the Ellipses

Transmission spectra were recorded as a function of the angle of polarization of the incident light, taken in steps of 10°. The spectra collected are similar to the pair shown in Figure 5.4. The heights of the peaks at 790 nm and 620 nm are plotted as a function of polarization angle in Figure 5.6. For ellipse rotations of 0°, 15°, and 30°, Figure 5.6 shows a clear sinusoidal dependence of the peak intensity on the polarization angle of the incident

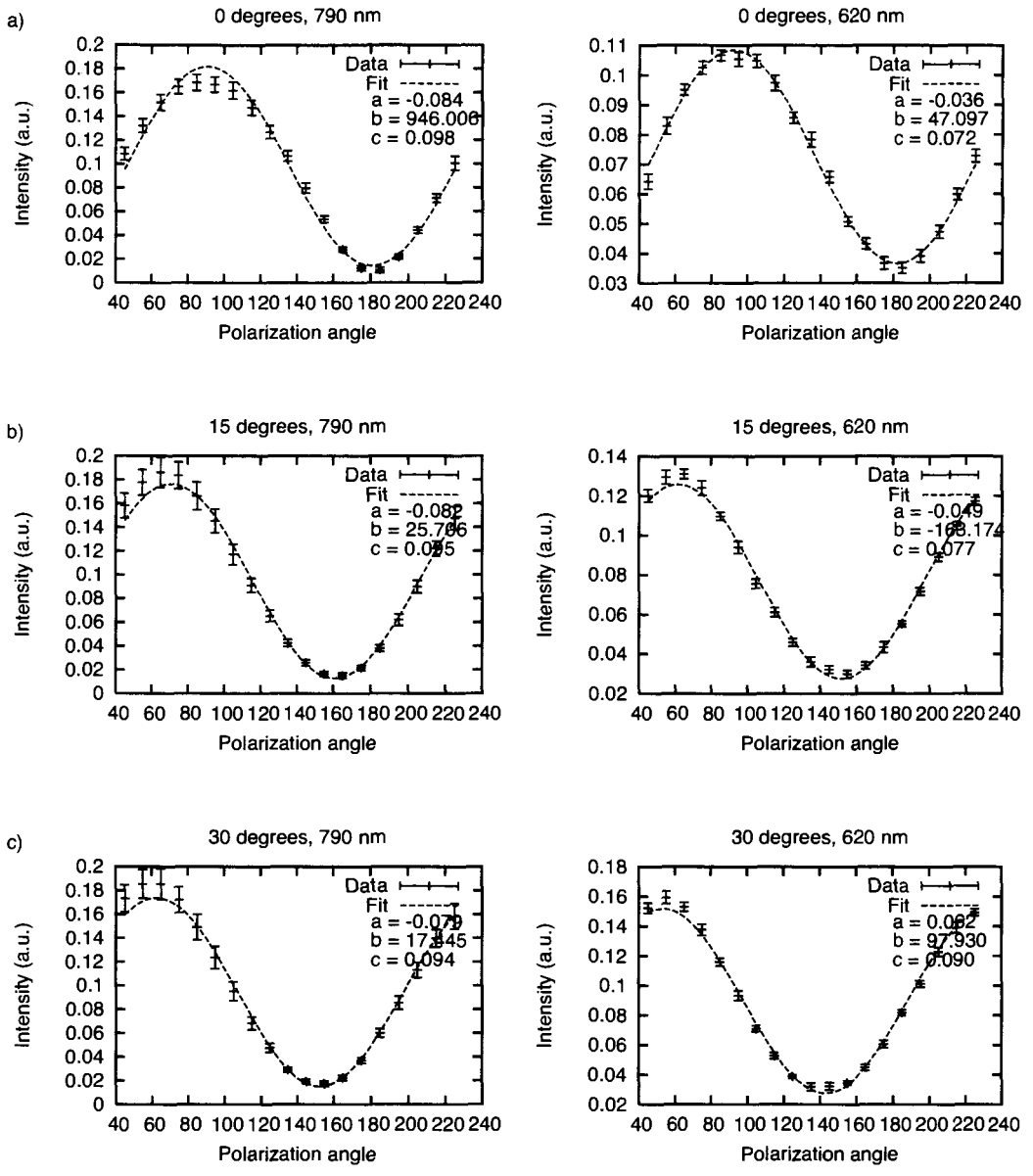


Figure 5.6: Intensity of the transmission peaks at 790 nm and 620 nm, for elliptical nanoholes as a function of the polarization angle of the incident light (with respect to the [1,0] axis) for ellipses rotated at a) 0°, b) 15°, and c) 30°. A polarization angle of 90°corresponds to p-polarized light. The dashed lines are cosine fits to the data.

light. The transmission intensity varies with the sine of the angle between the major axis of the ellipse and the polarization of the incident light. The maximum transmission always occurs when the polarization is perpendicular to the major axis. From this series of plots, it follows directly that the polarization of maximum transmission follows the major axis of the ellipse. The peak intensities in each of the above mentioned plots, were fit as a function of polarization angle to a cosine curve, and overlaid on each graph.

$$-a\,cos\left(\frac{2\pi}{180}(x-b)\right)+c \tag{5.1}$$

A plot of the phase of these cosine fits as a function of ellipse orientation is shown in Fig. 5.9.

### 5.3.3 Offset of the Double Holes

In a manner similar to the ellipses, spectra were collected from the double hole arrays, varying the polarization of the incident light from 0°to 180°, in steps of 10°. Two transmission spectra are shown in Figure 5.7. The solid and dashed line respectively correspond to the $(\Delta X, \Delta Y)$ = (0,3R) and $(\Delta X, \Delta Y)$ = (3R,3R) double hole arrays. From the (0,3R) spectra to the (3R,3R) spectra, the 790 nm peak decreases and the 620 nm peak increases. The fact that the (3R,3R) array is similar to an array of single holes, with half the spacing, is then a convincing argument that the 790 nm peak and 620 nm peak are respectively associated with the (1,0) air-gold surface-plasmon mode, and the (2,0) glass-gold mode. The absolute intensity of the double hole spectra is more than twice as large as it is for the ellipses. This is consistent with the fact that the double holes are larger in area, by roughly a factor of two. The peak intensity plots were also fit to a cosine function (eq. 5.1), and the results shown in Fig. 5.9.

The polarization dependence for the double holes is quite different from that of ellipses. In the case of an array of elliptical nanoholes, the polarization of maximum transmittance follows the rotation axis of the ellipse, for both the 790 and 620 nm peaks. In the case of the double holes, the maximum transmission of the 790 nm peak occurs always when the polarization is in the [1,0] direction, and for the 620 nm peak, in the [1,1] direction. This dichotomy is demonstrated in Fig. 5.9, where the parameters of the fit to equation (5.1) are plotted. For ellipses, the phase increases with increasing angle, and the amplitude remains

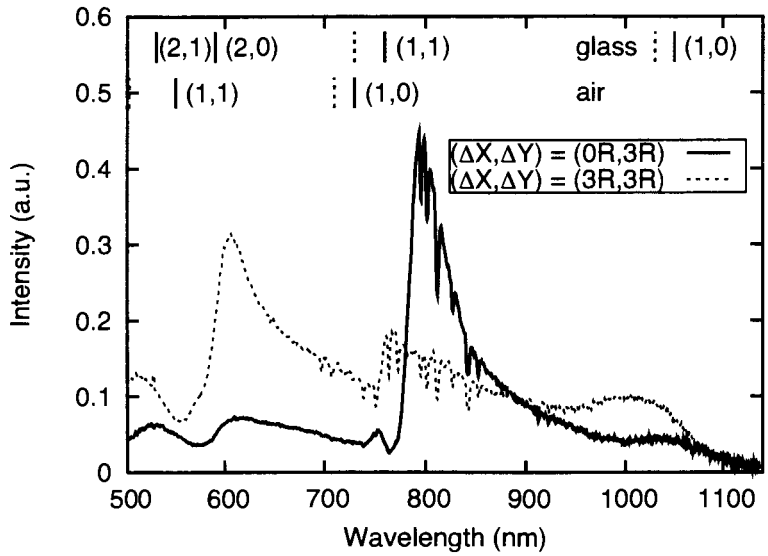


Figure 5.7: Sample Transmission Data for Double Holes. The solid line corresponds to a spectrum collected from the $(\Delta X, \Delta Y)$ = (0,3R) array, and the dashed line corresponds to a spectrum collected from $(\Delta X, \Delta Y)$ = (3R,3R) array. In both cases, the light is polarized 45°to the x-axis. The notches come from background illumination in the spectra that was somewhat smoothed using a boxcar average.

constant. For the double holes however, the phase remains constant, and the amplitude varies.

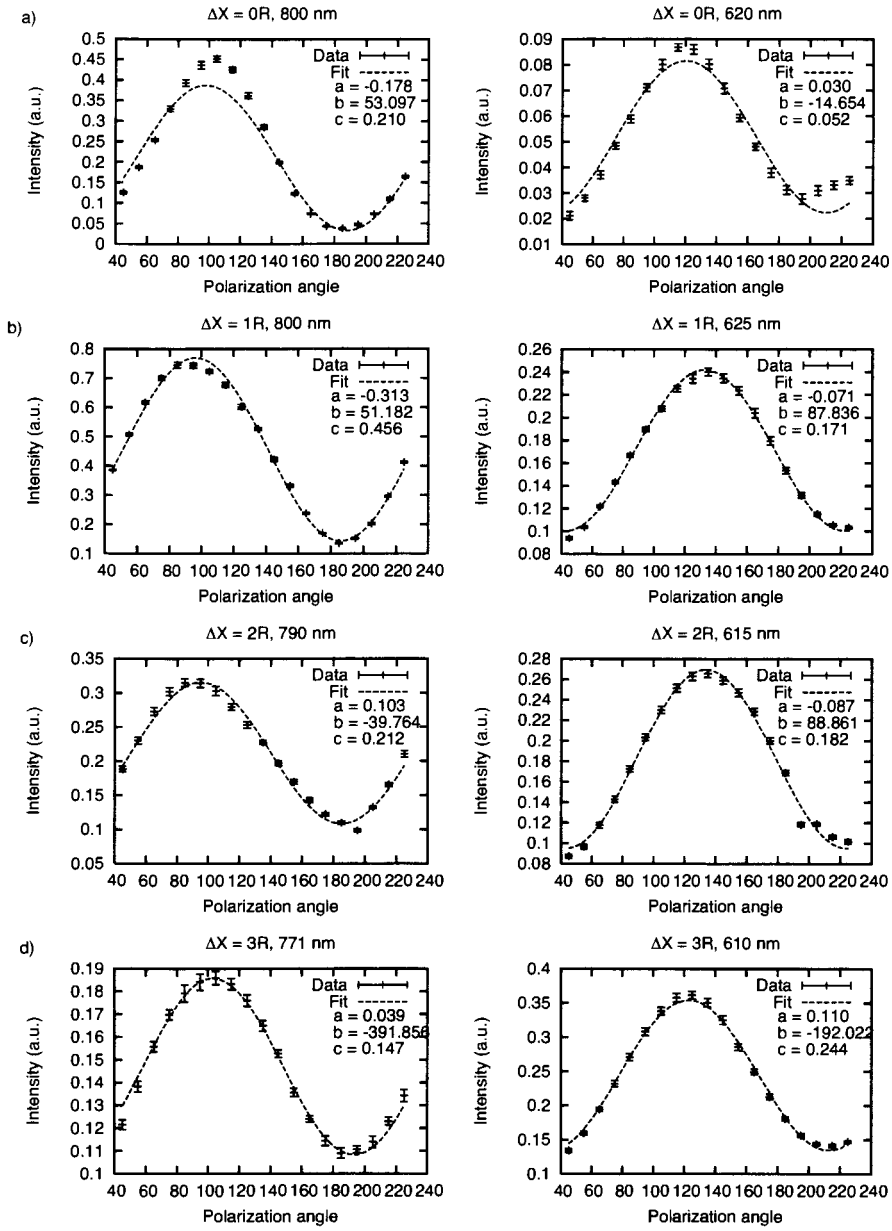


Figure 5.8: Intensity of the transmission peaks at 790 nm and 620 nm, for double hole nanoholes as a function of the polarization angle of the incident light (with respect to the [1,0] axis) for double holes offset at a) $\Delta X = 0R$, b) $\Delta X = 1R$, c) $\Delta X = 2R$ and d) $\Delta X = 3R$. The dashed lines are cosine fits to the data.

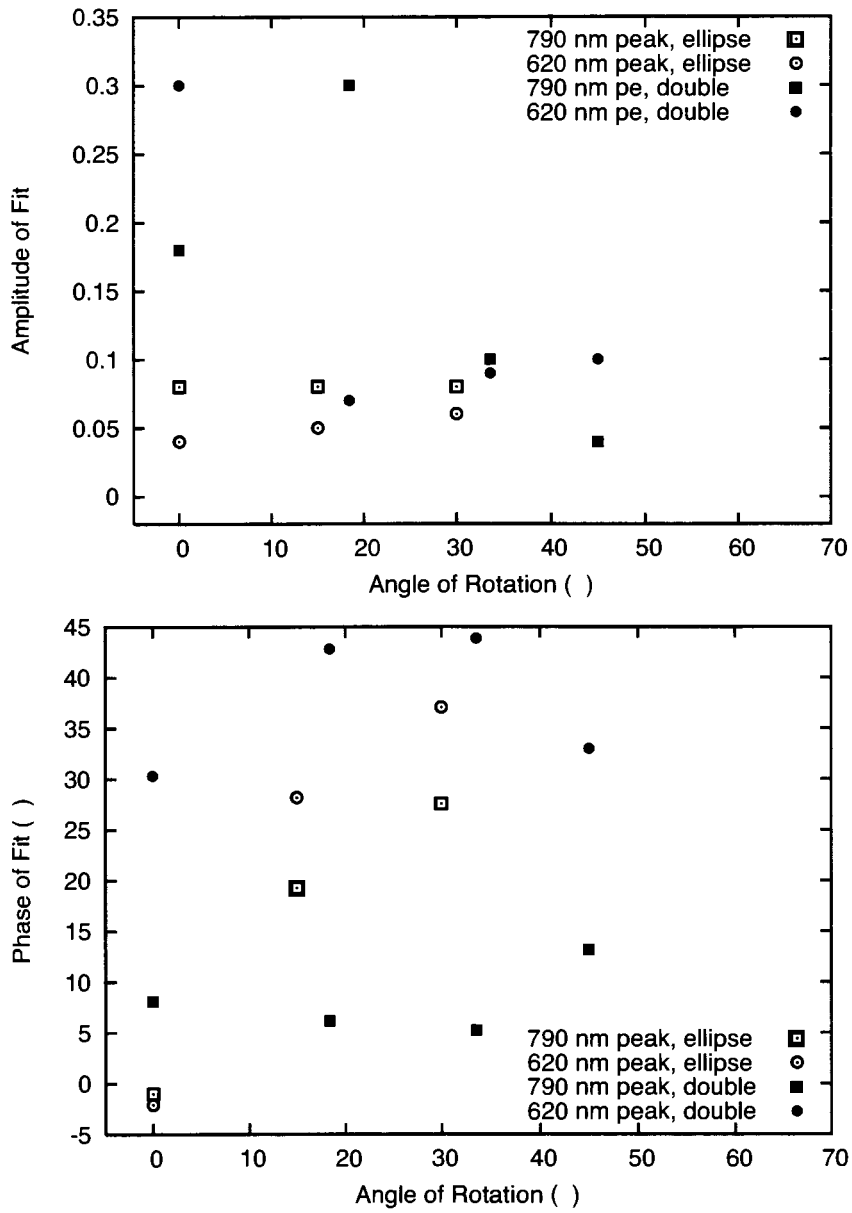


Figure 5.9: Coefficients of the cosine fits (eq. 5.1) to the data of Figs. 5.6 and 5.8 as a function of the polarization angle of the incident light.

# Chapter 6

# Analysis and Discussion

## 6.1 Simulations

The idea that the enhancement effect is explained by surface-plasmon-enhanced diffraction [11], is investigated by comparing the trends of the Fourier transform of the nanohole arrays with the trends observed experimentally. The amplitude of the diffracted field is proportional to the Fourier transform of the grating, and the intensity is proportional to the square of the amplitude. If the intensity of the diffracted wave is enhanced by the surface plasmons, then the trends observed experimentally should be seen in the square of the Fourier transform of the arrays.

### 6.1.1 Fourier Transforms

Two-dimensional Fourier transforms are taken of images of the surface. Rather, they are taken of idealized images of the surface. The Fourier transform equations,

$$\begin{aligned} H(\omega) &= \int_{-\infty}^{\infty} h(t) e^{2\pi i f t} dt \\ f(t) &= \int_{-\infty}^{\infty} H(\omega) e^{-2\pi i f t} dt \end{aligned} \tag{6.1}$$

bring one from the time domain to the frequency domain, and vice versa [29]. Similarly, one can go from real-space to $k$-space.

$$F(k) = \frac{1}{\sqrt{2\pi}} \int_{-\infty}^{\infty} f(x) e^{ikx} dx$$

$$f(x) = \frac{1}{\sqrt{2\pi}} \int_{-\infty}^{\infty} F(k) e^{-ikx} dx \tag{6.2}$$

Functions (6.1) work well when one is dealing with continuous functions; however, a different approach is used when dealing with discrete functions.

$$h_k \equiv h(t_k), \qquad t_k \equiv k\Delta, \qquad k = 0, 1, 2, \ldots, N-1 \tag{6.3}$$

where $\Delta$ is the sampling interval. We then have a discrete sample of the continuous function $h(t)$. Approximating the integrals (6.1) as discrete sums gives the discrete Fourier transform, and its inverse [29].

$$\begin{aligned} H_n &= \sum_{m=0}^{N-1} h_k e^{2\pi imn/N} \\ h_m &= \frac{1}{N} \sum_{n=0}^{N-1} H_n e^{2\pi imn/N} \end{aligned} \tag{6.4}$$

The Fast-Fourier-Transform (FFT) is the algorithm that reduces the number of operations required to perform a Fourier transform from $O(N^2)$ to $O(N \log_2 N)$. Consider the Fourier transform of a discrete function f

$$F_n = \sum_{m=0}^{N-1} f_m e^{2\pi imn/N} \tag{6.5}$$

We can split the Fourier sum into its even and odd components

$$\begin{aligned} F_n &= \sum_{m=0}^{N-1} e^{2\pi imn/N} f_m \\ &= \sum_{m=0}^{N/2-1} e^{2\pi in(2m)/N} f_{2m} + \sum_{m=0}^{N/2-1} e^{2\pi in(2m+1)/N} f_{2m+1} \\ &= \sum_{m=0}^{N/2-1} e^{2\pi inm/(N/2)} f_{2m} + W^m \sum_{m=0}^{N/2-1} e^{2\pi inm/(N/2)} f_{2m+1} \\ &= F_n^{even} + W^k F_m^{odd} \end{aligned} \tag{6.6}$$

where $W \equiv e^{2\pi i/n}$. The transform of length N has been reduced to the sum of two transforms of length N/2. If N is a power of 2, then we can recursively apply this technique $log_2 N$

times. The FFT can then be expressed as the sum of transforms of length 1. However, the Fourier transform of length one is just the identity transform. As a result, one can write

$$F_m^{eoeoooeeeeo\cdots eoeo} = f_n \tag{6.7}$$

So each of the terms in this sum for the Fourier transform is just one of the values of the initial function to be transformed. The key to solving the problem lies in the fact that the value sequence of e's and o's is a binary number (where e = 1, o = 0) that corresponds to the value $f_n$. Thus, computing the Fourier Transform has been reduced to a problem in bookkeeping.

### 6.1.2 Generation of the Images

Idealized images of the arrays of nanoholes were created in C using the PNG library. It is required that the images of the array tile, that is if the image is repeated in the x or y direction, the spacing of the lattice is continuous across the image boundary. This is important to prevent artifacts appearing in the Fourier transform with a spatial wavelength equivalent to the size of the image.

In addition to tiling, the idealized images of the arrays must have a size of $2^N \times 2^N$ pixels. This puts a requirement on the spacing of the array to also be of the form $2^m$, or else the image will not tile.

It would be ideal if the stream files used to create the arrays in the FIB could be used to create the idealized images. However, the arrays in the stream files have a spacing of 100 pixels, which is not a power of two. As a result, idealized images were created using a lattice spacing of 128 pixels. The major and minor axis of the ellipses was kept the same as the stream files, at 20 and 10 pixels, respectively. An example of an idealized image is shown in Fig. 6.1

## 6.2 FFT Results

The FFTs were created originally using code from the "Numerical Recipes in C" [29]. However, the pre-existing libraries in MATLAB were found to perform the task well. A MATLAB script was created to read in a series of PNG image files and perform the FFT. FFT images were created, and the various reciprocal lattice values were recorded.

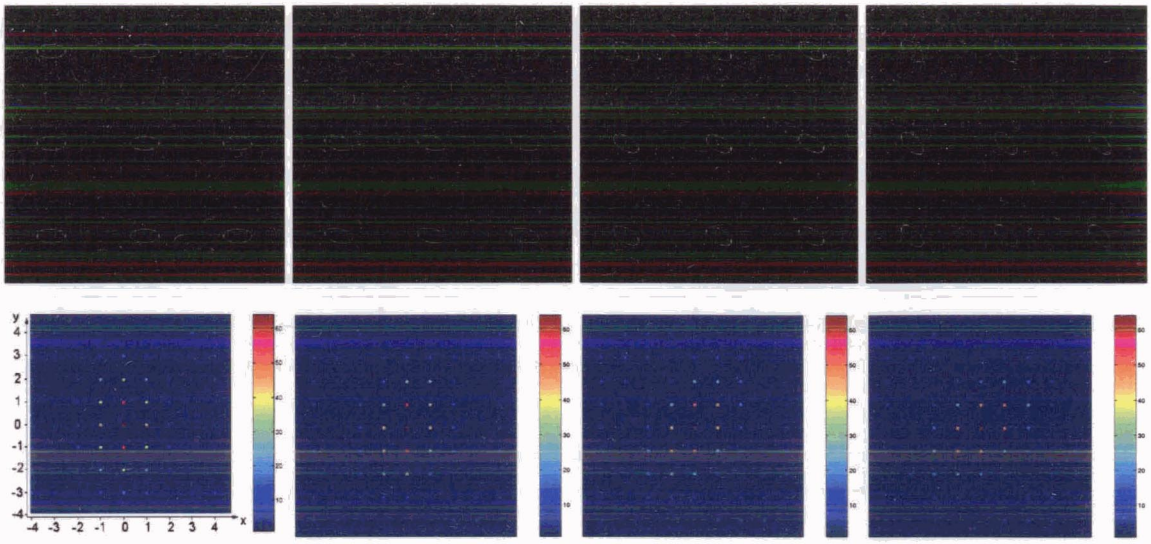

(a) 0 degrees (b) 15 degrees (c) 30 degrees (d) 45 degrees

Figure 6.1: Images of idealized elliptical nanohole arrays, and the corresponding images of the FFT transforms, where the elliptical nanoholes are set at various angles of rotation.

### 6.2.1 FFTs of Ellipses

Ellipses with a major axis of 20 pixels, and a minor axis of 10 pixels were created in a lattice with a spacing of 128 pixels, with varying angles of rotation. Using a 1024x1024 array of 64 ellipses, gives the FFTs in Fig. 6.1. The lattice of points in the FFT is associated with the lattice in the idealized images. The overall intensity modulation of the lattice points is caused by the ellipses at each of the lattice points of the idealized images. The FFT image is seen to rotate with the rotating basis of the lattice (see Fig. 6.1). If we take the center point of the FFT images as the origin, we then define the (1,0), (0,1) (1,1) and (1,-1) reciprocal lattice points from this origin. These reciprocal lattice points indicate how the light of different polarizations will interact with the lattice. For instance, p-polarized light (perpendicular to the major axis of the ellipse) will have its electric field vector pointing in the [0,1] direction.

To compare with the experimental data, plots were made of the intensity of the (1,0) and

(0,1) reciprocal lattice points as a function of the ellipse rotation angle, as shown in Figure 6.2. The squares in the plot correspond to the array represented in a 1024 pixel × 1024 pixel image, while the crosses in the plot correspond to the same lattice, but scaled to a 4096 pixel × 4096 pixel image. Both arrays have the same number of elements, everything was merely scaled by a factor of four. From this comparison, we can see that the irregularities of the 1024×1024 plot at 10°, 35°, 55°, and 80°are artifacts of the discretization of the array, as they decrease in amplitude as the resolution is increased. All subsequent plots were created from arrays with a resolution of 4096×4096 pixels.

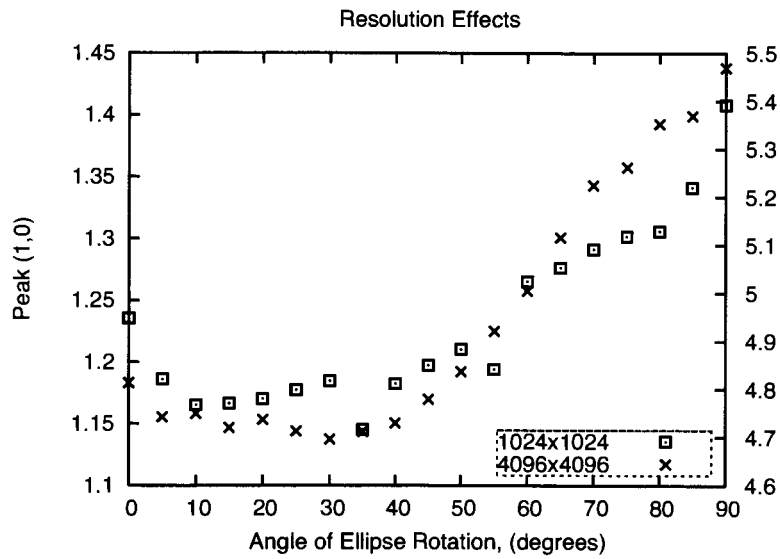


Figure 6.2: Amplitude of the (1,0) peak from the FFT analysis of elliptical arrays as a function of the rotation of the ellipses. The two plots correspond to the same array represented at two different resolutions 1024x1024 pixels and 4096x4096 pixels.

An attempt was made to ascertain whether it is just the edge of the hole that is relevant to the enhancement process, or if a consideration of the area of the hole was more appropriate. To this end, the FFT calculations were carried out both on a series of arrays of solid and empty elliptical nanoholes. Figure 6.4a shows the (1,0) and (0,1) amplitude for empty holes, while Figure 6.4c shows the amplitudes for filled holes. The overall trend is very similar for the two cases. The (0,1) reciprocal lattice point decreases in amplitude with increasing

polarization angle, while the (1,0) reciprocal lattice point amplitude increases.

Overlaid with the simulated data are the experimental data on both 6.4a) and b) for the (1,0) and (0,1) resonance, scaled appropriately. The agreement between the experimental data and the filled holes is much better than with the empty holes. If we compare the ratios of the (0,1) and (1,0) peaks (Figs.6.4c) and d), the two cases are almost indistinguishable, and agree well with the cosine dependence observed experimentally (Fig. 5.6).

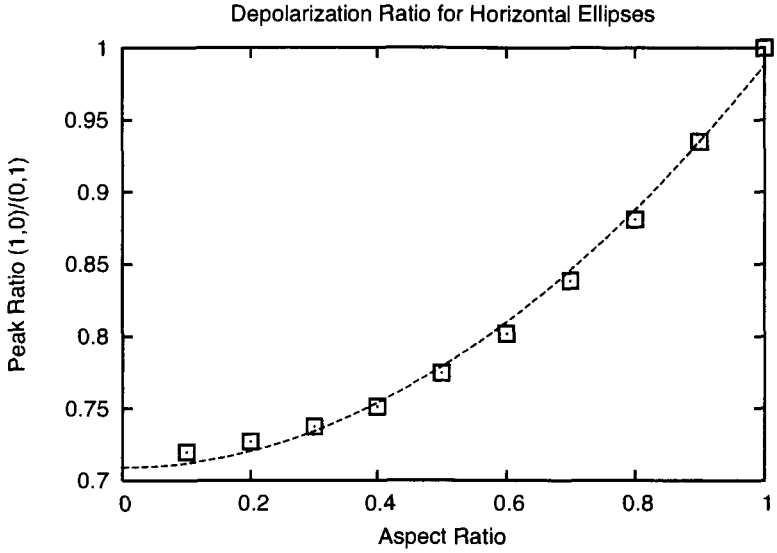


Figure 6.3: Depolarization ratio as a function of the hole aspect ratio

To further test the agreement between the Fourier transform results and the experimental data, a series of idealized arrays were created with varying aspect ratios. Fig. 6.3 demonstrates the parabolic dependence of the polarization on the aspect ratio of the holes. The agreement is quite strong with Fig. 5.5; however, the depolarization ratio for the FFT result does not go to zero as the aspect ratio of the ellipse collapses.

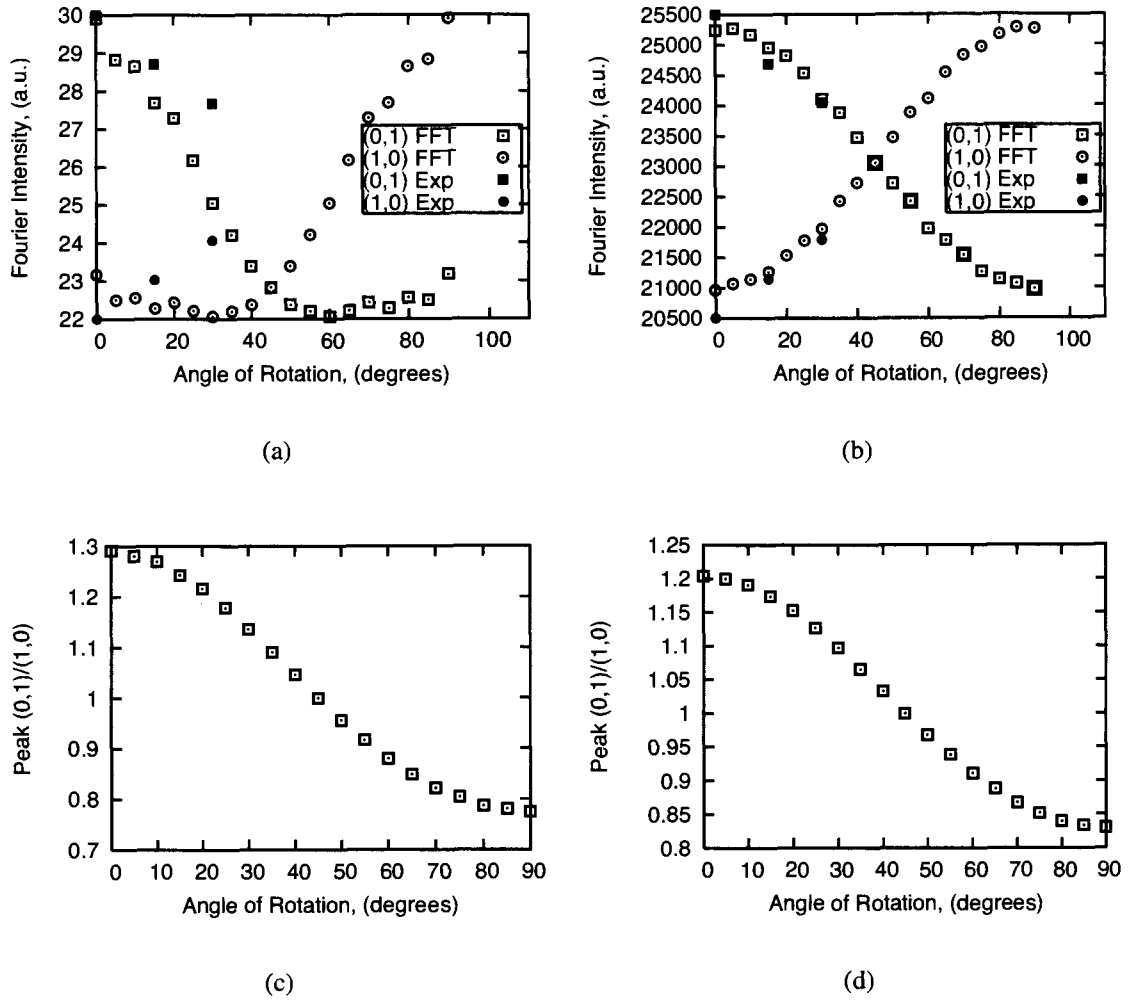


Figure 6.4: Plots of the intensity of the (0,1) and (1,0) reciprocal lattice points of the FFTs of arrays of ellipses, open symbols, as a function of ellipse rotation for a) empty ellipses and b) solid ellipses. The solid symbols are experimental data points. The (0,1) to (1,0) peak intensity versus angle of ellipse rotation are plotted in c) for empty ellipses and d) for solid ellipses.

### 6.2.2 FFTs of Double Holes

In a similar approach to the ellipses, FFTs of double hole patterns were also calculated. Pattern and FFT images are shown in Fig. 6.5. Plots of the resulting (1,0) and (0,1) amplitudes are found in Fig. 6.6. The difference between the filled and empty holes is only evident in the amplitude of the peaks, and the two cases are qualitatively the same. Some insight can be gained by noticing that the (0,1) amplitude remained constant. This indicates that the amplitude of the (0,1) resonance is insensitive to the change in the offset between the holes in the [1,0] direction.

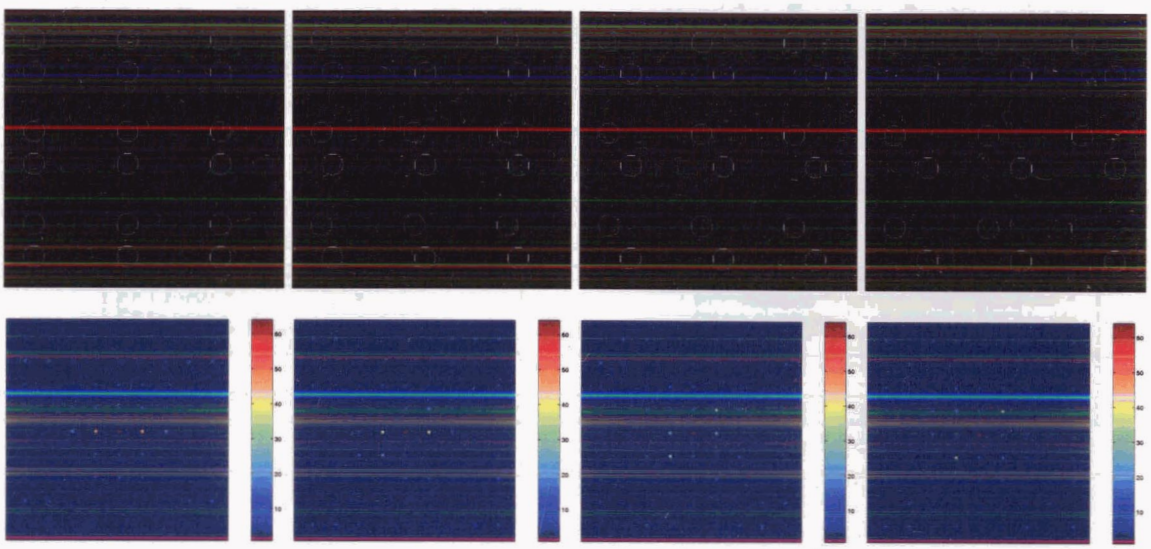

(a) $\Delta x = 0R$ (b) $\Delta x = 1R$ (c) $\Delta x = 2R$ (d) $\Delta x = 3R$

Figure 6.5: Images of idealized double-hole nanohole arrays, and the corresponding images of the FFT transforms, where the double-hole nanoholes are set at various amounts of x-offset.

While the FFT results do not fit the experimental data as nicely, the trends are the same. The (0,1) resonance, and the (0,1) reciprocal lattice point are both insensitive to the x-offset, while the (1,0) is sensitive. It is also possible that the $\Delta X = 15$ data point is an outlier, in which case the data and FFT results could be better scaled to match the experimental results.

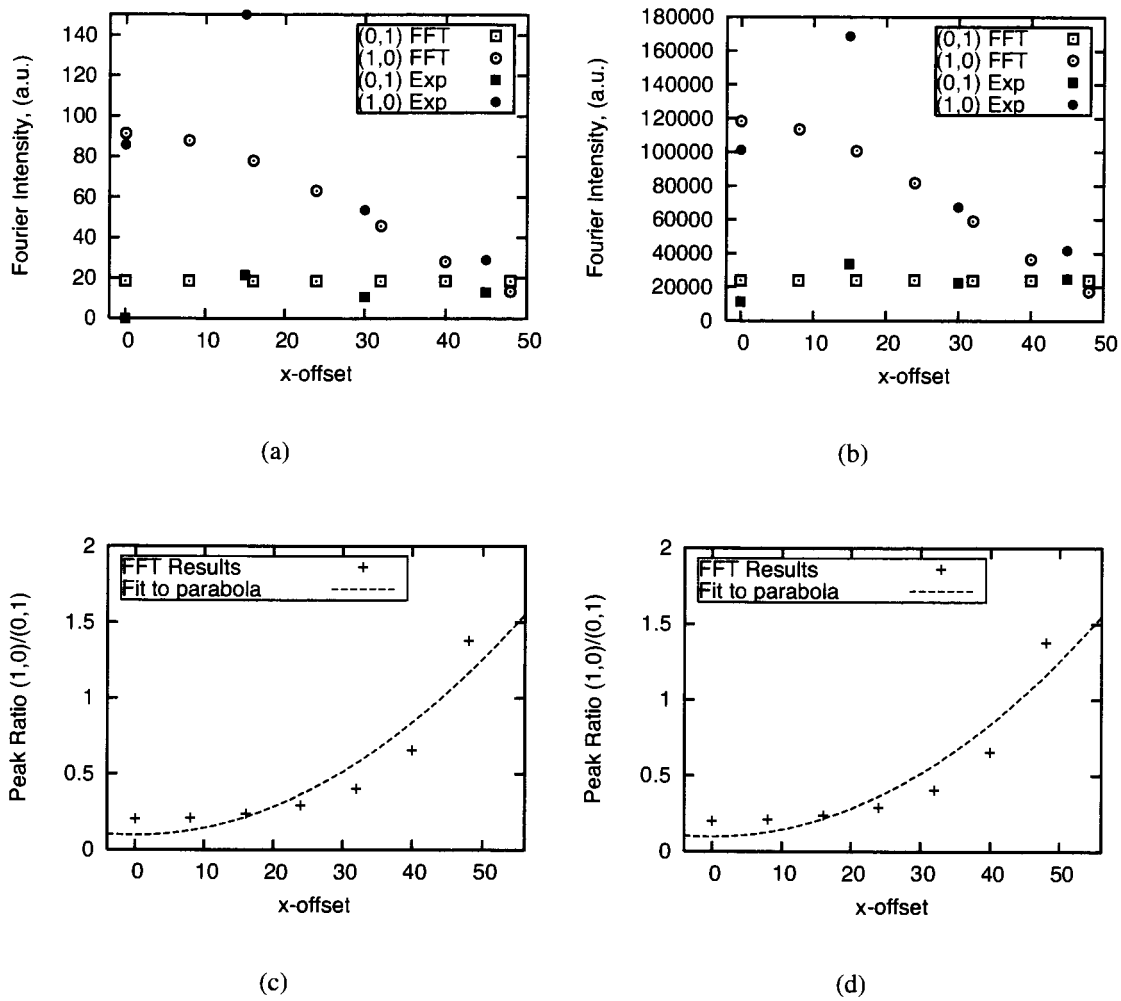


Figure 6.6: Plots of the (0,1) and (1,0) reciprocal lattice points of the FFTs of arrays of double holes, open symbols, as a function of x-offset for a) empty holes and b) solid holes. The solid symbols are experimental data points. The (0,1) to (1,0) peak intensity versus the x-offset are plotted in c) for empty holes and d) for solid holes.

# Chapter 7

# Conclusions

The STM-LE system designed, built, and tested did not succeed in detecting tunneling induced light emission. The difficulty in aligning the fiber optic with the point source of light at the STM tip proved to be more difficult than anticipated. However, this problem is surmountable by designing a new tip holder, directly incorporating the fiber optic, which can then couple optically to the photodetector.

A focused-ion beam was successfully manipulated to produce arrays of nano-sized holes of desired shape and size. Enhanced optical transmission through these arrays of nanoholes was observed, confirming previous results. A previously unknown dependence of the polarization of the transmitted light on the shape and orientation of the holes was observed. An analysis based on Fourier-transform techniques supports the idea that surface plasmons act to enhance the diffraction effect and hence give an increased transmission.

Future plans for the project involve filling the holes with various dielectric materials to study how they change the transmission spectra. Additionally, arrays will be fabricated on semiconductor substrates, to allow a coupling to various electro-optic devices. A novel approach to creating sensors by fabricating the arrays on the ends of fiber optic cables will also be investigated.

# Appendix A

# Program Code

## A.1 Program for Creating Elliptical Stream Files

The code of a program written in Python to create elliptical stream files. Instructions on its use can be found in Section 4.2.

```
#!/usr/bin/python

import math, array

def square(x):
    result = x * x
    return result

def Parse():
    ## read in the command line options
    from optparse import OptionParser
    usage="%prog␣[OPTIONS]␣FILE"

    parser = OptionParser(usage)
    parser.add_option("-x", "--x-axis", type="int", dest="xa
      ", default=10,
```

```
                    help="The␣length␣of␣the␣x-axis␣of␣the␣
                        ellipse.␣␣␣Default=10")

parser.add_option("-y", "--y-axis", type="int", dest="ya
    ", default=10,
                    help="The␣length␣of␣the␣x-axis␣of␣the␣
                        ellipse.␣␣␣Default=10")

parser.add_option("-s", "--spacing", type="int", dest="s
    ", default=75,
                    help="The␣spacing␣of␣the␣ellipses.␣␣␣
                        Default=75")

parser.add_option("-q", "--spacing2", type="int", dest="
    q", default=75,
                    help="The␣spacing␣of␣the␣2nd␣array␣of␣
                        ellipses.␣␣␣Default=75")

parser.add_option("-d", "--dwelltime", type="int", dest=
    "d", default=100,
                    help="Dwell␣time␣of␣the␣ion␣beam.␣␣␣
                        Default=100")

parser.add_option("-p", "--shape", type="int", dest="p"
    , default=0,
                    help="The␣basis␣shape;␣0␣:␣ellipse
                        ,␣1␣:␣rectangle␣␣Default=0")

parser.add_option("-a", "--angle", type="float", dest="a
    ", default=0,
                    help="Angle␣of␣rotation␣of␣the␣ellipse
                        (degrees).␣␣␣Default=0")
```

```
parser.add_option("-r", "--sparse", type="int", dest="r"
    , default=0,
                      help="Sparse Pattern; 0 : no, 1 : yes
                          Default=0")

parser.add_option("-l", "--loops", type="int", dest="l"
    , default=1,
                      help="The number of times to repeat
                          the pattern.   Default=1")

parser.add_option("-n", "--num", type="int", dest="n",
    default=1,
                      help="The number of shapes in the
                          basis, 1 or 2.   Default=1")

parser.add_option("-u", "--xoffset", type="int", dest="
    xo", default=15,
                      help="The x-offset of the second shape
                          in the basis.   Default=15")

parser.add_option("-v", "--yoffset", type="int", dest="
    yo", default=15,
                      help="The y-offset of the second shape
                          in the basis.   Default=15")

(options, args) = parser.parse_args()

try:
    args[0]
except IndexError:
    parser.print_help()
```

```
        return (1,None,options)
    else:
        return (0,args[0],options)

def Max(xa,ya):
    """ The maximum of two values """
    if xa > ya:
        max=int(xa)
    else:
        max=int(ya)
    return(max)

def Min(xa,ya):
    """ The minimum of two values """
    if xa < ya:
        max=int(xa)
    else:
        max=int(ya)
    return(max)

class Shape:
    def Define(self):
        """ Initialise some values for the while loop """
        shape=[]
        count=0

        i=-self.max_dim
        j=-self.max_dim
        while j < self.max_dim:
            while i <self. max_dim:
                #The rotated co-ordinates
```

```
                x=(i*math.cos(self.alpha)+j*math.sin(self.
                    alpha))
                y=(-i*math.sin(self.alpha)+j*math.cos(self.
                    alpha))
                if self.type == 0:
                    #Define an ellipse
                    if (square(x/self.xa) + square(y/self.ya
                        ) < 1):
                        if self.sparse==0:
                            shape.append((i,j))
                        elif (i-1,j) not in shape:
                            shape.append((i,j))
                elif self.type == 1:
                    #Define an square
                    if (math.fabs(x) < self.xa) and (math.
                        fabs(y) < self.ya):
                        if self.sparse==0:
                            shape.append((i,j))
                        elif (i-1,j) not in shape:
                            shape.append((i,j))
                else:
                    print "Invalid Shape specification ",
                        self.type
                    i=self.max_dim
                    j=self.max_dim
                i=i+1
            i=-self.max_dim
            j=j+1
        self.count=len(shape)
        return shape
```

```
    def __init__(self,xa, ya, angle, shape_type, sparse_bool
        ):
        self.xa = float(xa)
        self.ya = float(ya)
        self.alpha = math.radians(float(angle))
        self.max_dim = int(math.ceil(math.sqrt(pow(xa,2)+pow
            (ya,2))))
        self.gridmin = int(self.max_dim*2)
        self.gridmax = int(pow(2,12))-int(2*self.max_dim)
        self.count = None
        self.sparse = sparse_bool
        self.type = int(shape_type)
        self.shape = self.Define()

class Grid:
    def __init__(self):
        """The Grid container for the basis shapes """
        self.coords={}

    def AddPoint(self,xp,yp):
        self.coords[(xp,yp)]=1

    def Count(self):
        return len(self.coords)

    def Print(self):
        print self.coords

class Stream(Grid):
    def __init__(self,spacing,dwelltime,loops):
        """The container for the Grid, and file I/O"""
        self.grid=Grid()
```

```
        self.s=spacing
        self.d=dwelltime
        self.l=loops

    def Write(self,filename):
        spacer='          '
        eol='\r\n'
        f=open(filename,'wb')
        f.write('s'+eol+str(self.l)+eol+str(self.grid.Count
            ())+eol)
        keys=self.grid.coords.keys()
        keys.sort()
        for (xp,yp) in keys:
            f.write(str(self.d) + spacer + str(xp) + spacer
                + str(yp) + eol)
        f.close()

class Stream2(Grid):
    def __init__(self,spacing1,spacing2,xoffset,yoffset,
        dwelltime,loops):
        """The container for the Grid, and file I/O for a
            two element basis"""
        self.grid=Grid()
        self.s1=spacing1
        self.s2=spacing2
        self.xo=xoffset
        self.yo=yoffset
        self.d=dwelltime
        self.l=loops

#     def MaxCount(self,shape):
```

```
#           count_max=(shape.gridmax-shape.gridmin+1)//Min(self
    .s1,self.s2)
#           return (count_max)

    def Write(self,filename):
        spacer='          '
        eol='\r\n'
        f=open(filename,'wb')
        f.write('s'+eol+str(self.1)+eol+str(self.grid.Count
            ())+eol)
        keys=self.grid.coords.keys()
        keys.sort()
        for (xp,yp) in keys:
            f.write(str(self.d) + spacer + str(xp) + spacer
                + str(yp) + eol)
        f.close()

def CreateArray(filename,shape,stream):
    """Create the stream file [filename]"""

    xi,yi=0,0
    #count_max=stream.MaxCount(shape)

    gridmin=shape.gridmin
    gridmax=shape.gridmax
    spacing = stream.s
    x, y = gridmin, gridmin

    count_max=(gridmax-gridmin+1)//spacing


    while yi < count_max:
```

```
        while xi < count_max:
            for point in shape.shape:
                xp = gridmin + int(xi*spacing) + point[0]
                yp = gridmin + int(yi*spacing) + point[1]
                stream.grid.AddPoint(xp,yp)
            xi=xi+1
        yi=yi+1
        xi=0

    stream.Write(filename)

###

def CreateArray2(filename,shape,stream):
    """Create the stream file [filename], for a two element
       basis"""

    gridmin = shape.gridmin
    gridmax = shape.gridmax
    spacing1 = stream.s1
    spacing2 = stream.s2

    count_max1=(gridmax-gridmin+1)//spacing1
    count_max2=(gridmax-Max(stream.xo,stream.yo)-gridmin+1)
       //spacing2
    count_max=Max(count_max1,count_max2)

    count1_prediction=count_max1**2*shape.count
    count2_prediction=count_max2**2*shape.count

### A warning if two many points are in the stream file, NOT
    USED
```

```
#     while (count1_prediction+count2_prediction > 10**6-1):
#         print "Warning, number of lines is ",
    count1_prediction+count2_prediction, "1,000,000"
#         print "There are currently ", count_max1, "elements
     in array1"
#         print "There are currently ", count_max2, "elements
     in array2"
#         print "Reducing the number of lattice points..."
#         print ""
#         gridmax=gridmax-Min(spacing1,spacing2)
#         count_max1=(gridmax-gridmin+1)//spacing1
#         count_max2=(gridmax-Max(stream.xo,stream.yo)-
    gridmin+1)//spacing2
#         count_max=Max(count_max1,count_max2)

#         count1_prediction=count_max1**2*shape.count
#         count2_prediction=count_max2**2*shape.count

    print "Calculating the grid... "
    xi,yi=0,0
    count1, count2 = 0,0
    x, y = gridmin, gridmin

    while yi < count_max:
        while xi < count_max:
            for point in shape.shape:
                if xi < count_max1 and yi < count_max1:
                    xp = gridmin + int(xi*spacing1) + point
                        [0]
                    yp = gridmin + int(yi*spacing1) + point
                        [1]
                    stream.grid.AddPoint(xp,yp)
```

```
                    count1 = count1 + 1
            for point in shape.shape:
                if xi < count_max2 and yi < count_max2:
                    xp = gridmin + int(xi*spacing2) + point
                        [0] + stream.xo
                    yp = gridmin + int(yi*spacing2) + point
                        [1] + stream.yo
                    stream.grid.AddPoint(xp,yp)
                    count2 = count2 + 1
            xi=xi+1
        yi=yi+1
        xi=0

    count = count1 + count2

    print "writing␣the␣file..."

    stream.Write(filename)

    print "Lines␣in␣Array␣1:"
    print "␣␣␣␣␣␣␣␣expected:", count1_prediction
    print "␣␣␣␣␣␣␣␣␣␣actual:", count1
    print "Lines␣in␣Array␣2:"
    print "␣␣␣␣␣␣␣␣expected:", count2_prediction
    print "␣␣␣␣␣␣␣␣␣␣actual:", count2
    print "Lines␣in␣␣␣Total:"
    print "␣␣␣␣␣␣␣␣expected:", count1_prediction+
       count2_prediction
    print "␣␣␣␣␣␣␣␣␣␣actual:", stream.grid.Count()

def Main():
    parse=Parse()
```

```
    if parse[0]==0:
        filename=parse[1]
        O=parse[2]
        if (O.n==1): ### A single array
            stream=Stream(O.s,O.d,O.l)
            basis=Shape(O.xa,O.ya,O.a,O.p,O.r)
            CreateArray(filename,basis,stream)
        elif (O.n==2): ### A double array
            stream=Stream2(O.s,O.q,O.xo,O.yo,O.d,O.l)
            basis=Shape(O.xa,O.ya,O.a,O.p,O.r)
            CreateArray2(filename,basis,stream)
Main()
```

# Bibliography


[1] H. Bethe. Theory of diffraction by small holes. *Physical Review*, 66(7,8):163, 1944.

[2] R. Gordon, A.G. Brolo, A. McKinnon, A. Rajora, B. Leathem, and K.L. Kavanagh. Strong polarization in the optical transmission through elliptical nanohole arrays. *Physical Review Letters*, 92(3):037401, 2004.

[3] T. W. Ebbesen, H. J. Lezec, H. F. Ghaemi, T. Thio, and P. A. Wol. Extraordinary optical transmission through sub-wavelength hole arrays. *Nature*, 391:667, 1998.

[4] H.F. Ghaemi, T. Thio, Grupp D.W., T.W. Ebbesen, and H.J. Lezec. Surface plasmons enhance transmission through subwavelength holes. *Physical Review B*, 58(11):6779, 1998.

[5] T. Thio, H.F. Ghaemi, H.J. Lezec, P.A. Wolf, and T.W. Ebbesen. Surface-plasmon-enhanced transmission through hole arrays in Cr films. *Journal of the Optical Society of America B*, 16(10):1743, 1999.

[6] D.W. Grupp, H.J. Lezec, T.W. Ebbesen, K.M. Pellerin, and T. Thio. Crucial role of metal surface in enhanced transmission through subwavelength apertures. *Applied Physics Letters*, 77(11):1569, 2000.

[7] L. Martin-Moreno, F.J. Garcia-Videal, H.J. Lezec, K.M. Pellerin, T. Thio, J.B. Pendry, and T.W. Ebbesen. Theory of extraordinary optical transmission through subwavelength hole arrays. *Physical Review Letters*, 86:114, 2001.

[8] A. Degiron, H.J. Lezec, W.L. Barnes, and T.W. Ebbesen. Effects of hole depth on enhanced light transmission through subwavelength hole arrays. *Applied Physics Letters*, 81(23):4327, 2002.

[9] H.J. Lezec, A. Degiron, E. Devaux, R.A. Linke, L. Martin-Moreno, F.J. Garcia-Vidal, and T.W. Ebbesen. Beaming light from a subwavelength aperture. *Science*, 297:820, 2002.

[10] Eloise Devaux and Thomas W. Ebbesen. Launching and decoupling surface plasmons via micro-gratings. *Applied Physics Letters*, 83(24):4936, 2003.

[11] W.L. Barnes, W.A. Murray, E. Devaux Dintinger, and T.W. Ebbesen. Surface plasmon polaritons and their role in the enhanced transmission of light through periodic arrays of subwavelength holes in a metal film. *Physical Review Letters*, 92(10):107401, 2004.

[12] C. Sönnischsen, A.C. Duch, G. Steininger, M. Koch, and G. von Plessen. Launching surface plasmons into nanoholes in metal films. *Applied Physics Letters*, 76(2):140, 2000.

[13] M. Sarrazin, J.-P. Vigneron, and J.-M. Vigoureux. Role of Wood anomalies in optical properties of thin metallic films with a bidimensional array of subwavelength holes. *Physical Review B*, 67:085415, 2003.

[14] J.H. Coombs, J.K. Gimzewski, B. Reihl, J.K. Sass, and R.R. Schlittler. Photon emission experiments with the scanning tunneling microscope. *J. Microscopy*, 152(2):325, 1988.

[15] D.L. Abraham, A. Veider, Ch. Schönenberg, D.J. Arent, H.P. Meier, and S.F. Alvarado. Nanometer resoulution in luminescence microscopy of III-V heterostructures. *Appl. Phys. Lett.*, 56(16):1564, 1990.

[16] C. Kittel. *Introduction to Solid State Physics*. John Wiley and Sons Inc., 7th edition, 1996.

[17] H. Raether. *Surface Plasmons*, volume 111 of *Springer Tracts in Modern Physics*. Springer-Verlag, Berlin, 1988.

[18] Masud Mansuripur. *Classical Optics and its Applications*. Cambridge University Press, 2002.

[19] A. A. Talin, D. A. A. Ohlberg, R. S. Williams, P. Sullivan, I. Koutselas, B. Williams, and K. L. Kavanagh. Time dependent ballistic electron emission microscopy studies of a Au/(100)GaAs interface with a native oxide diffusion barrier. *Applied Physics Letters*, 62(23):2965, 1993.

[20] *Thorlabs http://www.thorlabs.com/.*

[21] J.K. Gimzewski, B. Reihl, J.H. Coombs, and R.R. Schlittler. Photon emission with the scanning tunneling microscope. *Z. Phys. B*, 72:497, 1988.

[22] *Newport Optics http://www.newport.com.*

[23] Masayuki Iwami, Yoichi Uehara, and Suketa Ushioda. Relation between the radius of tip curvature and the light emission efficiency from scanning tunneling microscope. *Japanese Journal of Applied Physics*, 39(8):4912, 2000.

[24] Paul Chafe. Electrochemical etching of W and Pt-Ir STM tips. Technical report, Simon Fraser University, 2002.

[25] Edward D. Palik, editor. *Handbook of Optical Constants of Solids*. Academic Press Inc., 1985.

[26] FEI Company, 7451 NW Evergreen Parkway. *xP Dual Workstation User's Guide*, 1999.

[27] Reuven Gordon. Department of Electrical and Computer Engineering at the University of Victoria.

[28] Alexandre G. Brolo. Department of Chemistry at the University of Victoria.

[29] W.T. Press, W. T. Vettering, S. A. Teukosky, and B. P. Flannery. *Numerical Recipes in C*. Cambridge University Press, 2nd edition, 1992.